ELECTRONIC PROPERTIES OF GRAIN BOUNDARIES IN SILICON

by

D.J. Thomson

A thesis

presented to the University of Manitoba

in partial fulfillment of the

requirements for the degree of

Master of Science

in

Electrical Engineering

Winnipeg, Manitoba, 1982

ELECTRONIC PROPERTIES OF GRAIN BOUNDARIES IN SILICON

BY

DOUGLAS J. THOMSON

A thesis submitted to the Faculty of Graduate Studies of the University of Manitoba in partial fulfillment of the requirements of the degree of

MASTER OF SCIENCE

Abstract

An experimental investigation is reported of carrier transport across isolated grain boundaries in large-grain cast silicon material. The importance of including, into the transport model, limitations on the supply of majority carriers by diffusion to the grain boundary is suggested by the present results. Continuous interface-state densities in the 10^{15} to 10^{16} $m^{-2}eV^{-1}$ range are measured for the lower part of the silicon energy gap. The grain-boundary diffusion potentials for this material are shown in some cases to vary appreciably over a single grain boundary plane; this is thought to be due to a nonuniform spatial distribution of interface charge at the grain boundaries. A theoretical model is developed for conduction across nonuniform boundaries relying on a Gaussian distribution of electrostatic potential. Comparisons of the model with experiment is made with favourable agreement.

An experimental investigation of majority-carrier grating solar cells, as originally proposed by Green, has been made and a comparison is drawn with minority-carrier cells fabricated and tested under identical conditions. The collecting junctions between the metal grid and the silicon represent 'peaked' Schottky barriers in the majority-carrier devices. Active-area efficiencies for AM1 Solar illumination (both simulated and natural sunlight) are 11.4% and 14.0% respectively for majority- and minority-carrier cells of ~1 cm^2 area on crystalline silicon. Spectral response data is also presented, and further comparisons are made with cast polycrystalline silicon grating solar cells, and with commercial diffused p-n junction solar cells.

Experimental observations are presented concerning the dependence of the spectral response of silicon photovoltaic cells upon the optical illumination intensity. These effects are significant only in silicon materials with many extended defects: grain boundaries and dislocations. In this case, the short-circuit current response to a chopped monochromatic optical excitation increases monotonically as a background optical (white light) bias is increased to approximately AM1 intensity. These results may be explained in terms of SRH recombination through defect states at grain boundaries and dislocations which under these conditions enter a high-injection regime at the defect sites, as a result of their associated space-charge regions. The mechanism helps to understand the observation that the photocurrents in solar cells made from cast polycrystalline silicon are not appreciably lower than for crystalline silicon.

Acknowledgements

Many thanks to my thesis advisor, Professor H.C. Card, for his guidance in my work, without his physical insight and communication skills my work would not have progressed as far as it did. I would also like to thank Professor Card for assisting me in my application to Stanford.

I would also like to acknowledge helpful discussions with my colleagues in the Materials and Devices Research Group, especially G.G. McGonigal, R.D. McLeod and A.W. De Groot. I would also like to thank G.C. McGonigal and R.D. McLeod for their aid in my experimental work.

Thanks also to Dr. F. Hawthorne (Department of Earth Sciences) for his help with the crystal alignments.

List of Figures

Fig. 2.11 Electron energy-band diagrams for grain boundary with (zero-bias) diffusion potential V_{do} . (a) $V = 0$; (b) $V > 0$. V_1 and V_2 are the portions of applied voltage V developed across the space-charge regions to the left and right of the grain boundary, respectively.

Fig. 2.12 Density of localized grain boundary interface states vs. energy in band gap of silicon (sample B-10). Points show results obtained from current-voltage characteristics at constant temperature T , for three values of T .

Fig. 2.13 Comparison of present results for grain-boundary interface states with earlier results for silicon grain boundaries (Refs. 26 and 27). Note units of N_{is} are $cm^{-2}eV^{-1}$ for this figure.

Fig. 2.14 Model of grain boundary for orientational mismatch of $\simeq 20°$, showing periodic nature of particular defect structure. Variety of bonding disorder is suggested over one period. Note repetition of approximately periodic disorder with a period of three atomic spacings along Canadian-American border.

Fig. 3.1 Band diagram of grain boundary with and without bias.

Fig. 3.2 Plot of $a(V_d)$ vs V_d for $< V_d > = 0.50$ and $\sigma = 0.08$.

Fig. 3.3 Plot of the kernel of integral (5) for $T = 300K$ and $T = 250K$ with $< V_d > = 0.50$ and $\sigma = 0.08$.

Fig. 3.4 Typical I-V characteristics of a nonuniform grain boundary (sample B-10) at several measurement temperatures.

Fig. 5.2 Spectral response (quantum efficiency) of minMIS solar cells made from p-type Wacker'Silso' cast polycrystalline silicon, and from crystalline Czochralski silicon. Obtained from short-circuit current measurements.

Fig. 5.3 Spectral response of minMIS solar cells made from p-type Wacker 'Silso' cast polycrystalline silicon, with the intensity of an optical bias (white light from GE ELH lamp) as a parameter (normalized to result in absence of optical bias, Fig. 2). Obtained from incremental response of short-circuit current to chopped monochromatic light of low intensity.

Fig. 5.4 Energy-band diagram in neighborhood of extended defect in Silicon (a) in equilibrium, and (b) under appreciable optical illumination. Superimposed on these figures is a schematic distribution of trap states, or recombination centers.

Fig. 5.5 Characteristics of grating solar cells; described in detail in Ref. (16). Note that a modest reduction in short-circuit current is experienced in changing from crystalline to Wacker silicon (curves (a) and (c) respectively).

TABLE OF CONTENTS

CHAPTER I

Introduction

Studies of the electronic properties of polycrystalline silicon, hereafter referred to as polysilicon, have recently been motivated by the applications for this material both in integrated circuits and in the fabrication of terrestrial solar cells.

The study of polycrystalline semiconductor materials was initiated circa 1950 by various researchers including Volger[1], Petritz[2], Vogel, Read, and Lovell[3], Taylor, Odell, and Fan[4]. Volger postulated that polycrystalline semiconductor thin films were composed of regions of high resistivity (grain boundaries) separating regions of low resistivity (crystalline grains). Taylor, Odell, and Fan[4] were the first to study single grain boundaries and to present a model for electronic conduction across grain boundaries. Their model for conduction was based on the mechanism of carrier diffusion through two opposing space charge regions. They also developed ideas concerning charge redistribution at the grain boundaries in order to explain the relatively high breakdown voltages observed in germanium bicrystals. Vogel, Read, and Lovell[3] performed an experimental investigation of recombination at grain boundaries. These authors concluded the existence of a significant number of recombination centers (traps) at the grain boundary but were unable to estimate their density quantitatively for lack of information on the nature of the traps.

The analysis of Petritz[2] dealt with the photoconductivity of polycrystalline semiconductor thin films. In his analysis, as in that of Volger[1], he considered the grain-boundary resistance to be

much higher than that of the crystalline regions. Petritz employed a transport model similar to Taylor et al[4], but assumed that thermionic emission, rather than diffusion, was the major limitation to the majority-carrier current flow. Petritz's work has been well accepted and was followed by a paper by Mueller[5] which also relied upon the thermionic-emission theory. Matare[6] also investigated germanium bicrystals and found that these bicrystals exhibited a significant photoresponse, even for photon energies smaller than the semiconductor energy gap. From these results he postulated that germanium displayed a significnt peak in the grain-boundary interface state density at E_v = 0.42 eV.

The subsequent work of Seto[7] was very significnt for the understanding of polycrystalline silicon, the earlier work having concentrated upon germanium. He studied the conductivity and mobility of polysilicon over a wide range of impurity doping concentrations. His results were interpreted in terms of the thermionic-emission theory which provided for substantial agreement between theory and experiment. One should note, however, that the diffusion theory will also produce predictions in agreement with Seto's experimental results.

Card and Yang[8] systematically analyzed carrier recombination in optically-illuminated polycrystalline semiconductors. They calculated the dependence of minority-carrier lifetime on doping concentration, grain size and grain-boundary interface state density. The model has been applied successfully to several semiconductors[9].

Seager, Pike, and Ginley performed theoretical calculations and several experimental investigations of isolated grain boundries in silicon.[10],[11],[12],[13] In this work, Seager et al assumed that

the thermionic-emission of majority carriers was the dominant mode of current flow.[10] Experimentally they observed varistor-like behaviour in silicon bicrystals and attributed this behaviour to a rapid decrease in the density of grain-boundary interface states with energy,[12] although field-assisted emission for these states may provide another explanation of their observations.

This thesis comprises (i) fundamental studies of grain boundaries in silicon, and (ii) the fabrication and analysis of photovoltaic (solar) cells on polysilicon material. The first two chapters deal with the fundamental optoelectronic properties of grain boundaries in polysilicon. In Chapter II a new model for electronic conduction across spatially-uniform grain boundaries is presented, together with experimental data from several isolated grain boundaries in cast silicon, under various conditions of optical illumination, temperature and bias voltage. In Chapter III a model is developed for conduction across grain boundaries with spatially-nonuniform electrostatic potential distributions. This model is based upon a Gaussian distribution of potential over the sample area, and has also been applied to the analysis of data from several grain boundaries.

Chapters IV and V discuss the fabrication and characterization of solar cells on crystalline and polycrystalline silicon. Details of the fabrication and testing are given as well as a comparison of metal-insulator-semiconductor (MIS) and PN-junction solar cells. In Chapter VI the high-injection condition at dislocations and grain boundaries in polycrystalline silicon is examined. Experiments are reported which concern the spectral response of a polysilicon solar cell under an optical bias of white light of up to 1 sun intensity.

Conclusions and recommendations for further work are given in the final chapter.

CHAPTER II

Electronic Transport at Grain Boundaries in Silicon*

2.1 Introduction

In the paper[13] by Shaw and Card they described the nature of grain boundaries in silicon, and in particular the carrier transport across these boundaries with the effects of bias-dependent charge in interface states. In this chapter we present the results of an experimental investigation of transport phenomena at grain boundaries in silicon. A number of excellent studies of a similar nature have been reported earlier by Seager et al[10-12,14]. The present work differs from these studies in several important ways.

A minor difference is that our investigations are of grain boundaries in p-type silicon so that the information obtained concerning grain-boundary interface states corresponds to the energy distribution of these states in the lower half of the energy gap, whereas Seager has obtained data for the upper half of the energy gap by using n-type silicon samples. We are also studying a somewhat different material: cast Wacker 'Silso' silicon, as opposed to their case of neutron-transmutation doped polycrystalline CVD silicon of somewhat smaller grain size and higher doping concentration. We further include in our study the cases of both high and low grain-boundary potential

---

*This chapter involved the collaboration of Mr. G.C. McGonigal; its contents have been submitted for publication to Physical Review B, October 1982.

barriers. Optical illumination intensity is employed in addition to bias voltage and temperature as experimental parameters: with the exception of some recent work concerning grain-boundary recombination velocity[8,14] most of the earlier studies involved dark measurements[10-12].

Finally, this chapter provides a necessary extension of previous work in its treatment of the data in terms of a generalized emission/diffusion model of carrier transport at grain boundaries. We are also led to the realization that, in the Wacker material at least, the grain-boundary potential can not be regarded as uniform over the grain boundary plane. Several other observations of a presently qualitative nature indicate that the carrier transport at grain boundaries can be a rather complex process.

2.2 Sample Fabrication and Measurements

The material used in this study was p-type cast silicon of large grain size (typically 1 mm) of the 'Silso' type, obtained from Wacker Chemitronic Ltd. The doping concentration N_a from bulk measurements (e.g. C^{-2} vs V of Schottky barrier capacitance-voltage characteristics for diodes within single grains) was $\simeq 3 \times 10^{21}$ m^{-3}. The polycrystalline wafers (100 mm x 100 mm x 0.4 mm) were cut into strips approximately 1 mm x 20 mm. These strips were chemically polished in 3:1:1 HNO_3 (79%), HF (49%), glacial acetic acid, for $\simeq$ 3 min. to eliminate saw damage and to highlight the grain boundaries[15]. Grain boundaries were examined under an optical microscope to identify those which were planar and which extended over the entire cross-section of

the strip in both the lateral and vertical directions; the latter requirement was determined by examining the back face of the samples.

Aluminum contacts were evaporated in a four-probe configuration (Fig. 2.1) and were sintered at 600°C for 20 mins in N_2 to form ohmic contacts. Aluminum connections were bonded to the (inner two) voltage measurement contacts. A single grain boundary was then enclosed between the voltage probes. Current was injected and removed at the outer two contacts. Contact potential errors in the determination of the voltage across the grain boundary were avoided by means of this four-probe technique; voltages were measured using a Keithley 610C electrometer with input impedance of 10^{11}ohms. All measurements were made under dc conditions.

Measurements at temperatures from 300K - 200K were performed in a FTS Multi-Cool closed-cycle refrigeration unit. For temperatures from 100K to 200K a cryogenic liquid nitrogen sample chamber fitted with a heater for temperature variation was employed. Temperatures were measured using Cu-Constantan thermocouples. Optical illumination was provided by a Sylvania ELH projection lamp with an infrared filter to remove all photon wavelengths $\lambda < 1$ μm. This ensured a relatively uniform photogeneration throughout the sample. The optical intensity was determined using an Optikon Model 550-1 radiometer. The accuracy of this determination was approximately ± 30%. The reflection from the silicon surface was estimated to be 30%.

The equilibrium grain-boundary diffusion potential, V_{do}, was observed to vary over a wide range for samples cut from different grain boundaries (V_{do} values from < 0.1 V (electrically inactive) to $\simeq 0.33$ V at 300K).

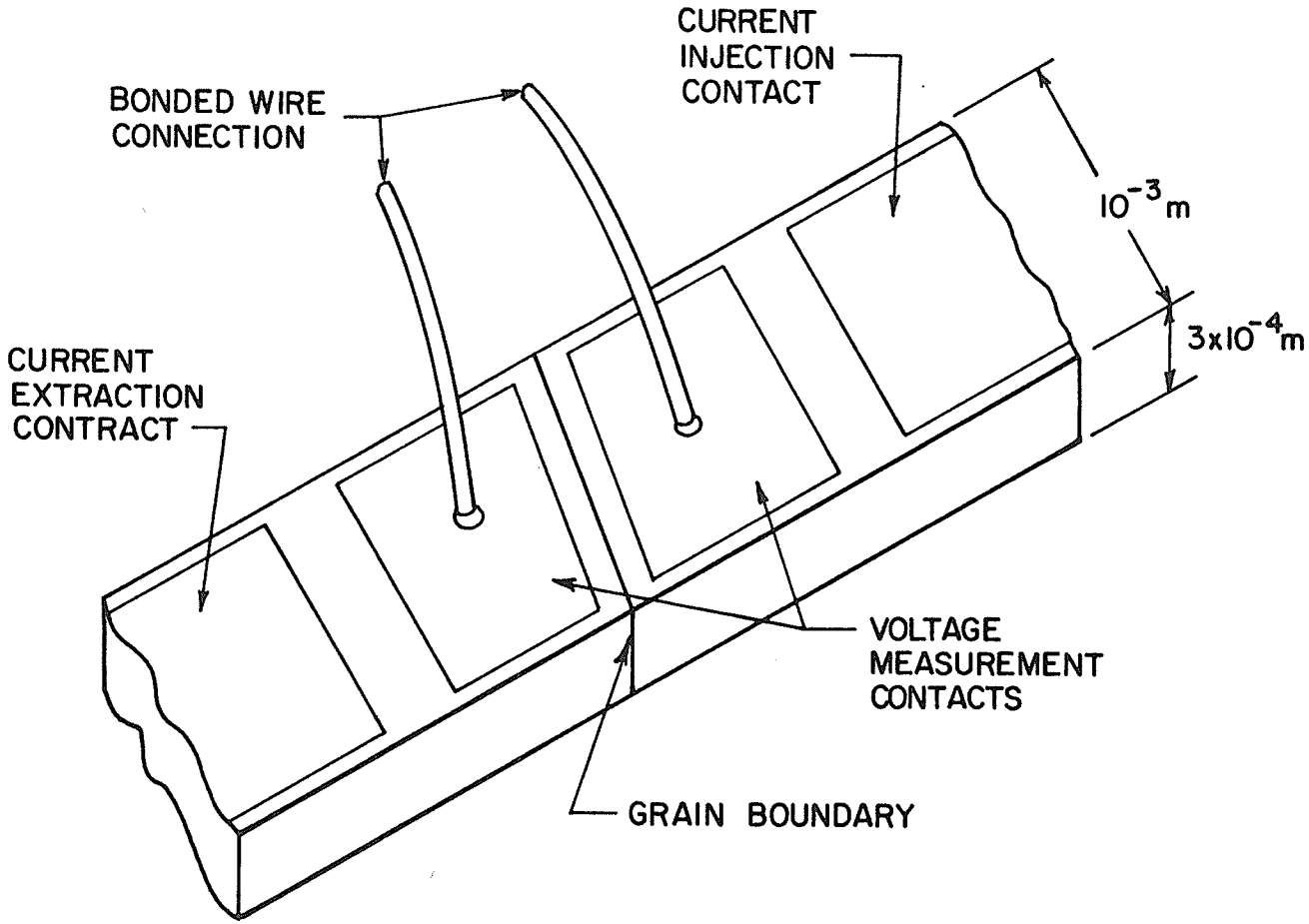

Fig. 2.1 Sample geometry. Cross sectional area of all samples ≈ 3 x 10^{-7} m^{-2}.

2.3 Experimental Results

Figure 2.2 shows a typical example of the current-voltage characteristics measured on a grain boundary having a relatively large zero-bias diffusion potential ($V_{do} \simeq 0.25$ V at 300K). Results are given for a number of measurement temperatures. Measurements such as these were performed for a variety of samples over the temperature range $100K \leq T \leq 300$ K. Figure 2.3 shows a typical example of the corresponding characteristics for a grain boundary with a somewhat smaller (zero bias) diffusion potential. These grain boundaries turn out to exhibit a spatial variation in their properties over the boundary plane. Figure 2.4 is representative of a different case of grain boundary in which the potential barrier is spatially uniform, as we discuss in a later section.

The effect of optical illumination on the grain-boundary current-voltage characteristics is illustrated in Figs. 2.5 and 2.6. This data was obtained for optical powers of 0.2 W m^{-2} and 50 W m^{-2} respectively with $1.0 \leq \lambda \leq 1.1$ μm. A range of optical illumination intensities was investigated, but the rather complicated behaviour observed at higher intensities is still under study at this time.

In Fig. 2.7 we show the dependence of the activation energy E_a (defined later) upon the voltage V applied across a boundary region. This activation energy is determined from the temperature dependence of the current-voltage characteristics such as those of Figs. 2.2-2.4. Figure 2.8(a) shows the dependence of E_a upon T (determined at a low value of V) for two of the same samples. From Fig. 2.8(a) and the expressions of Section 2.4 we are able to derive the equilibrium (dark, zero-bias) diffusion potential V_{do}, assuming

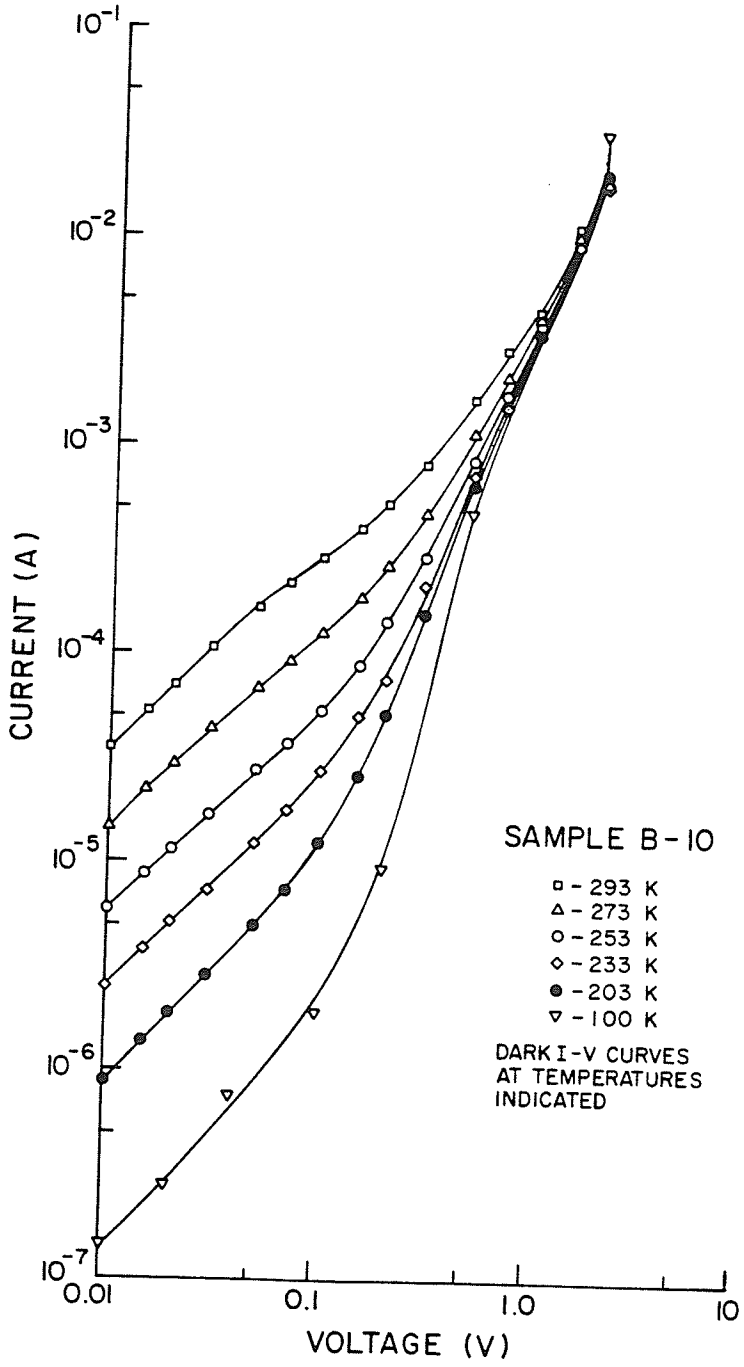

Fig. 2.2 Dark characteristics of grain boundary B-10 at several measurement temperatures.

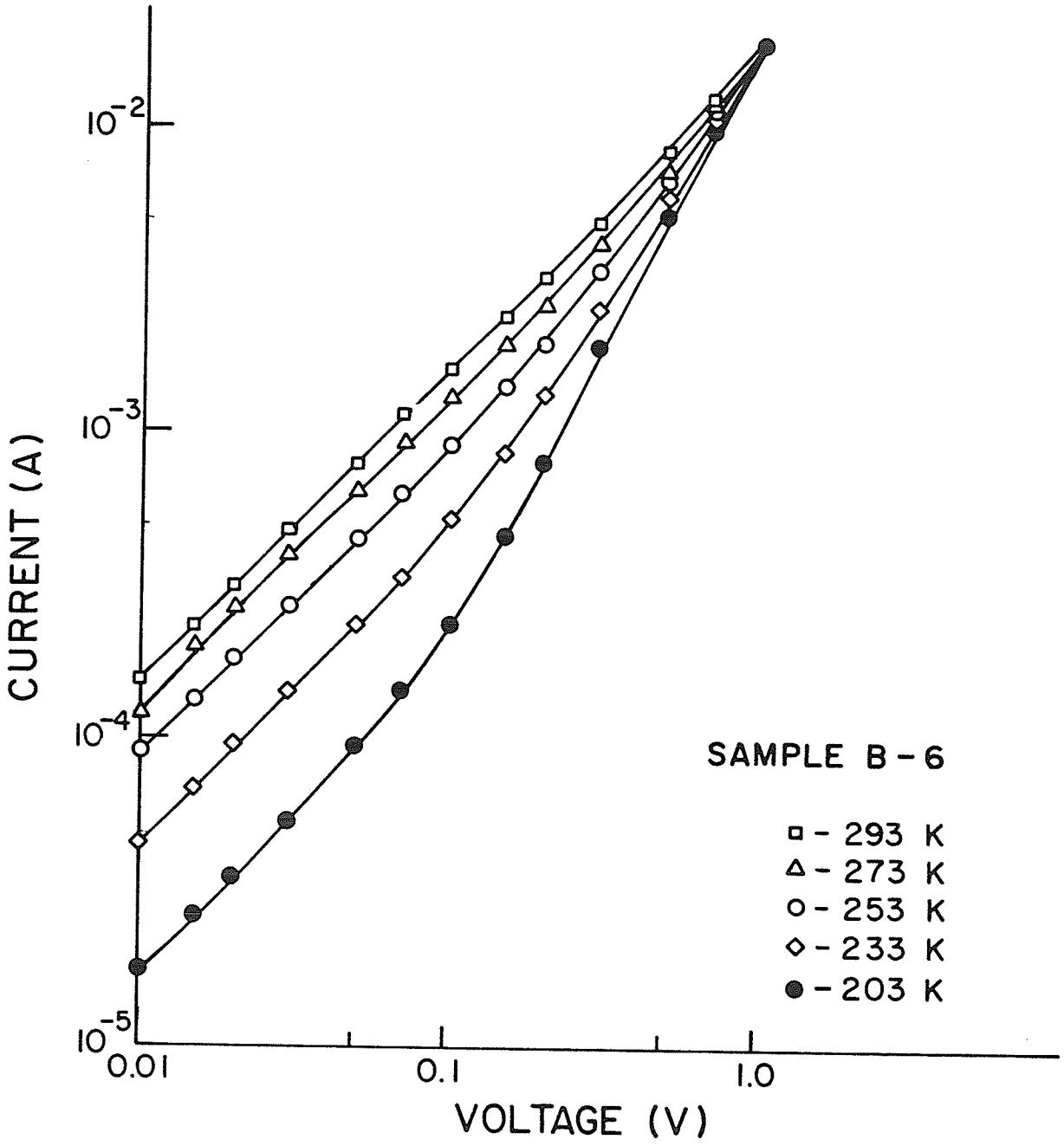

Fig. 2.3 Dark characteristics of grain boundary B-6 at several measurement temperatures.

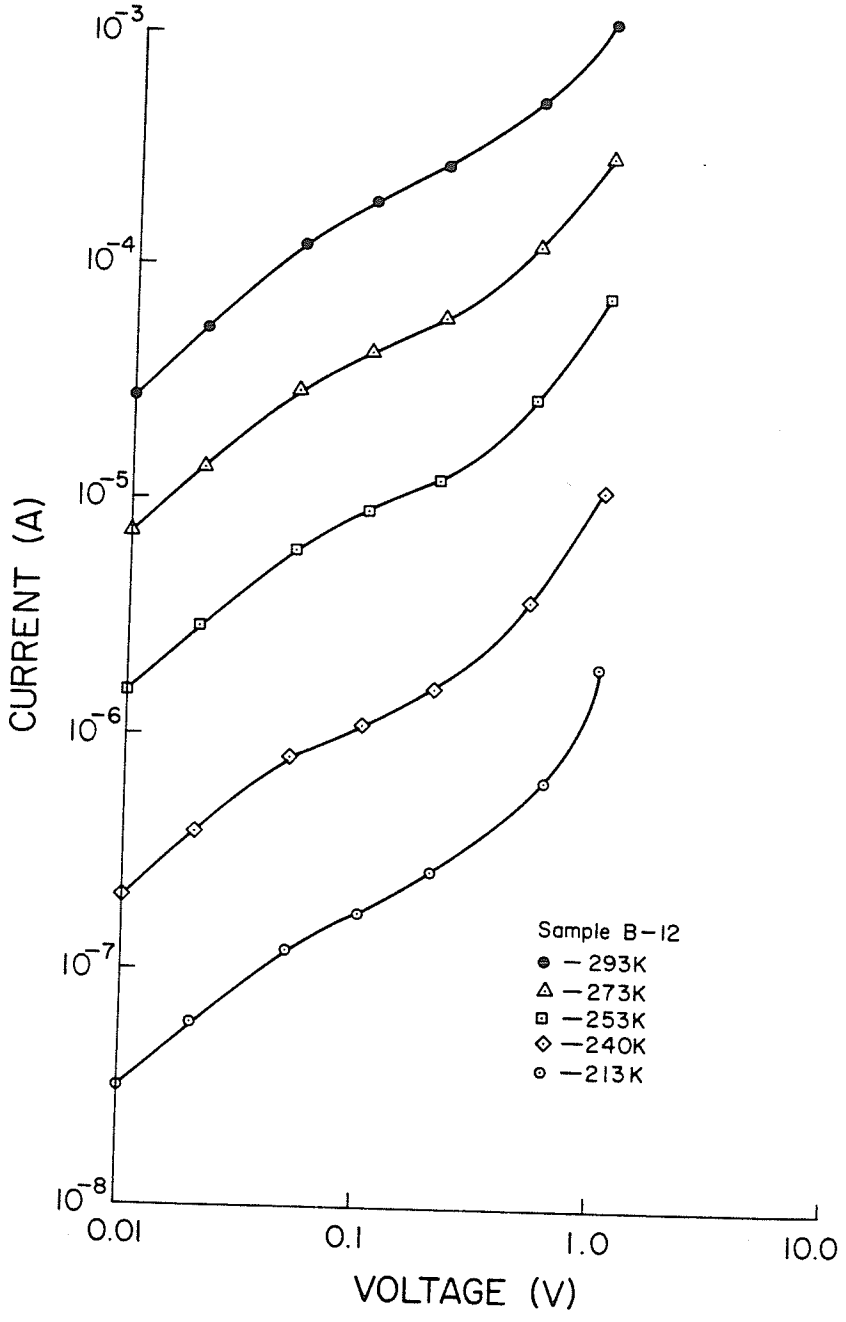

Fig. 2.4 Dark characteristics of grain boundary B-12 at several measurement temperatures.

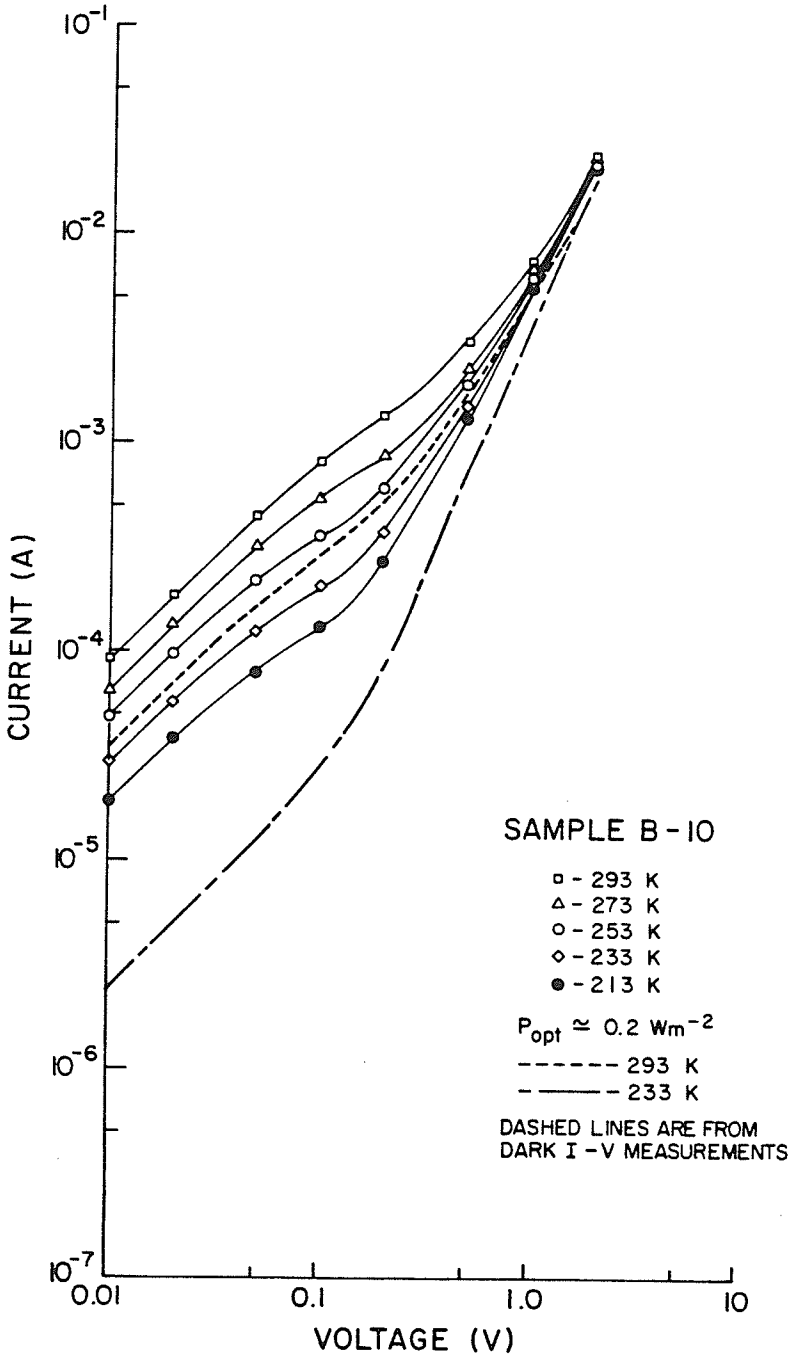

Fig. 2.5 Characteristics of B-10 under 0.2 W m^{-2} optical illumination ($1.0 < \lambda < 1.1\ \mu m$).

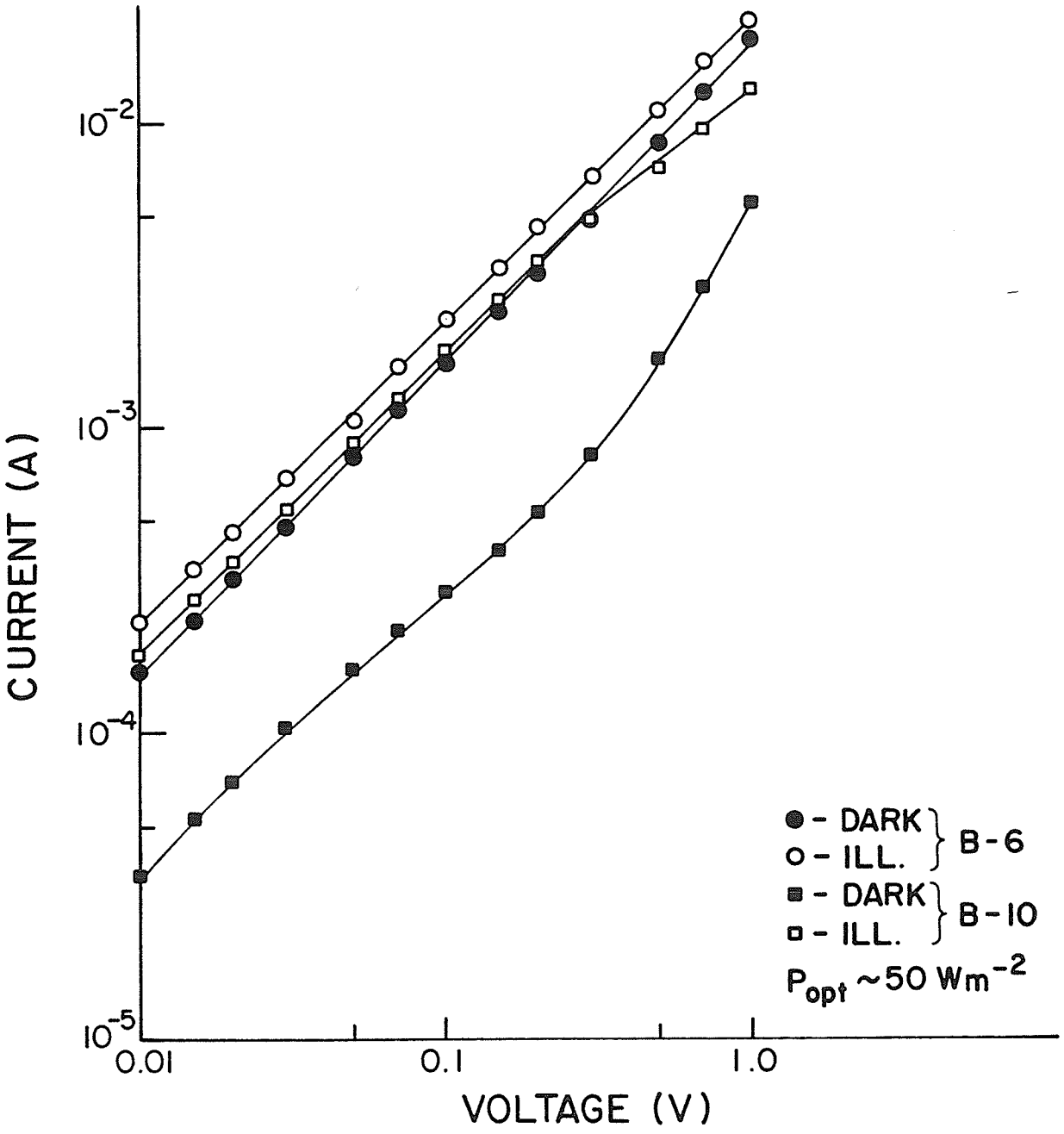

Fig. 2.6 Characteristics of B-6 and B-10 under 50 W m^{-2} ($1.0 < \lambda < 1.$ μm) optical illumination.

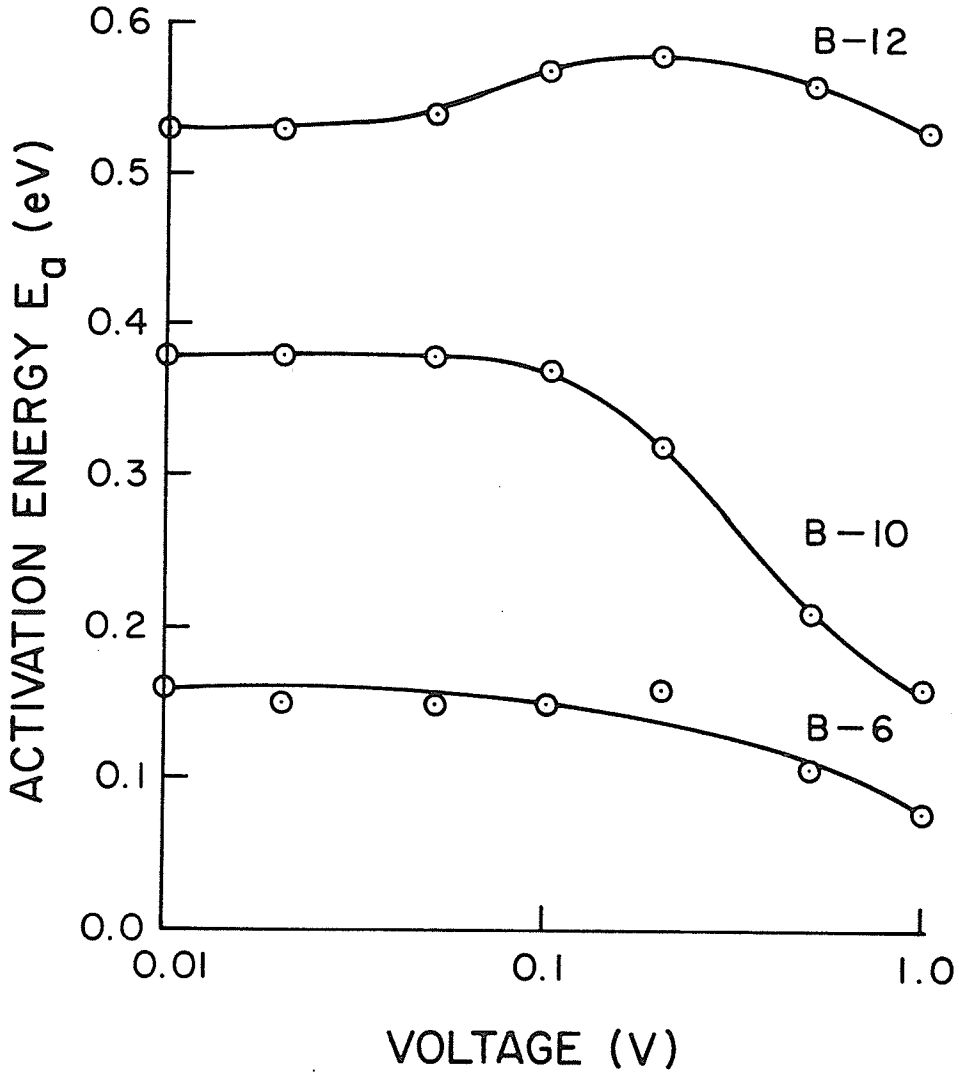

Fig. 2.7 Activation energy E_a vs. V applied to grain boundaries B-10, B-6 and B-12.

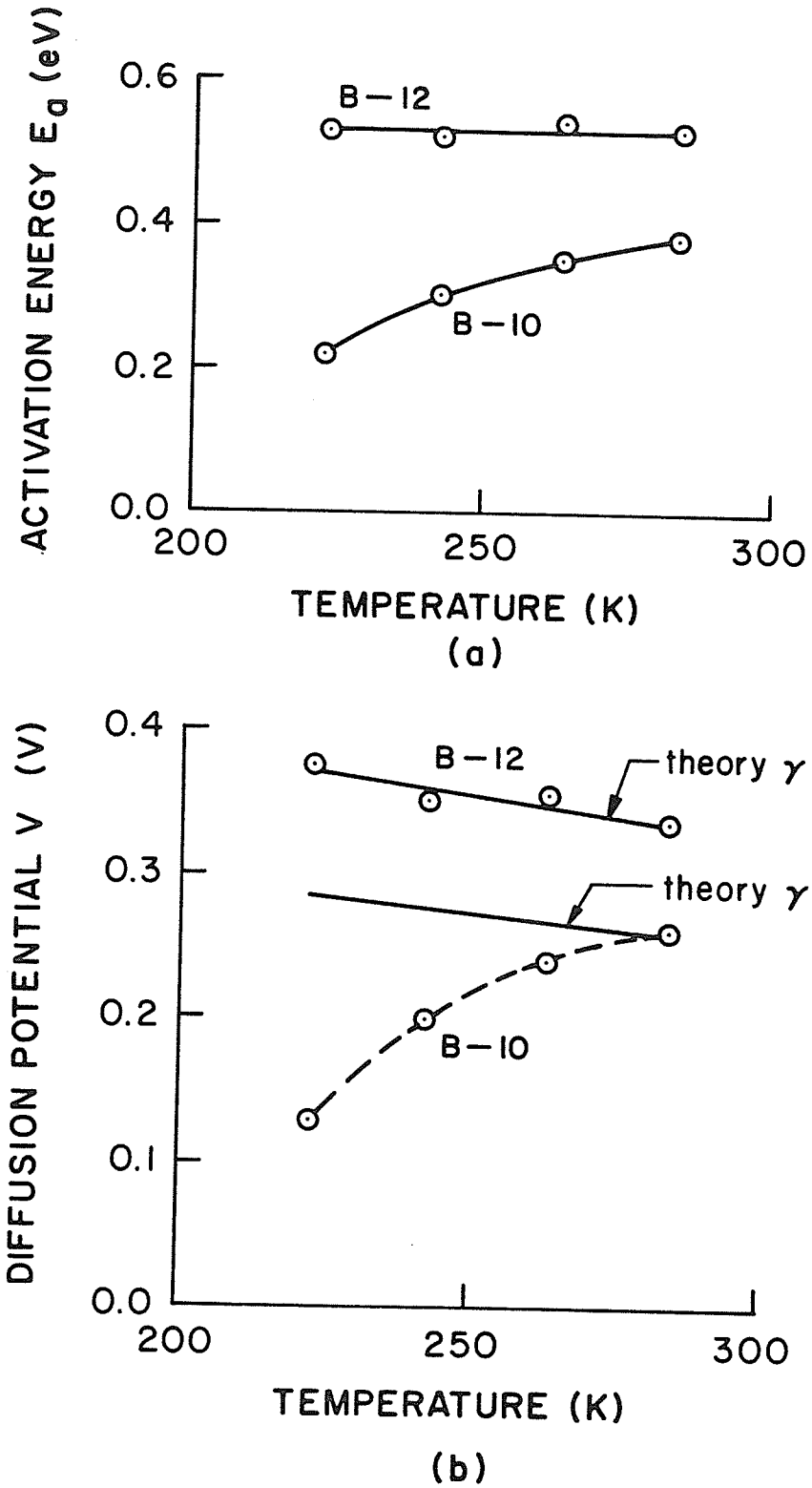

Fig. 2.8 The dependence of (a) the activation energy and (b) the diffusion potential on temperature for B-10 and B-12. In darkness.

that this potential is spatially uniform over the boundary plane. This is shown in Fig. 2.8(b), together with the result expected from a one-dimensional theory. Figures 2.9(a) and (b) give the observed dependence of E_a and V_d upon optical illumination intensity (at 300K) for the same samples. In this case V_d is no longer the equilibrium diffusion potential V_{do}.

It was also observed that for large grain-boundary voltages, and hence moderately large current densities ($\simeq$ 10-50V and 4×10^5 - 1×10^6 A m^{-2}) the current exhibited oscillations such as those shown in Fig. 2.10.

The magnitude of these oscillations was typically on the order of 1% of the dc current. It was observed that a sample biased below the threshold current density for these oscillations could be thermally stimulated into oscillation. Generally, more and larger pulses are observed at higher current densities, and these effects are reversible. We believe these oscillations are due to field emission of carriers from grain-boundary interface states, as discussed in a later section.

2.4 Modelling

In this section we present an analytical approximation to the numerical results of the paper by Shaw and Card[13], which is guided by those results. This approach provides an improved contact with the physics of grain-boundary phenomena, and a better understanding of the factors which are of primary importance in controlling the transport properties.

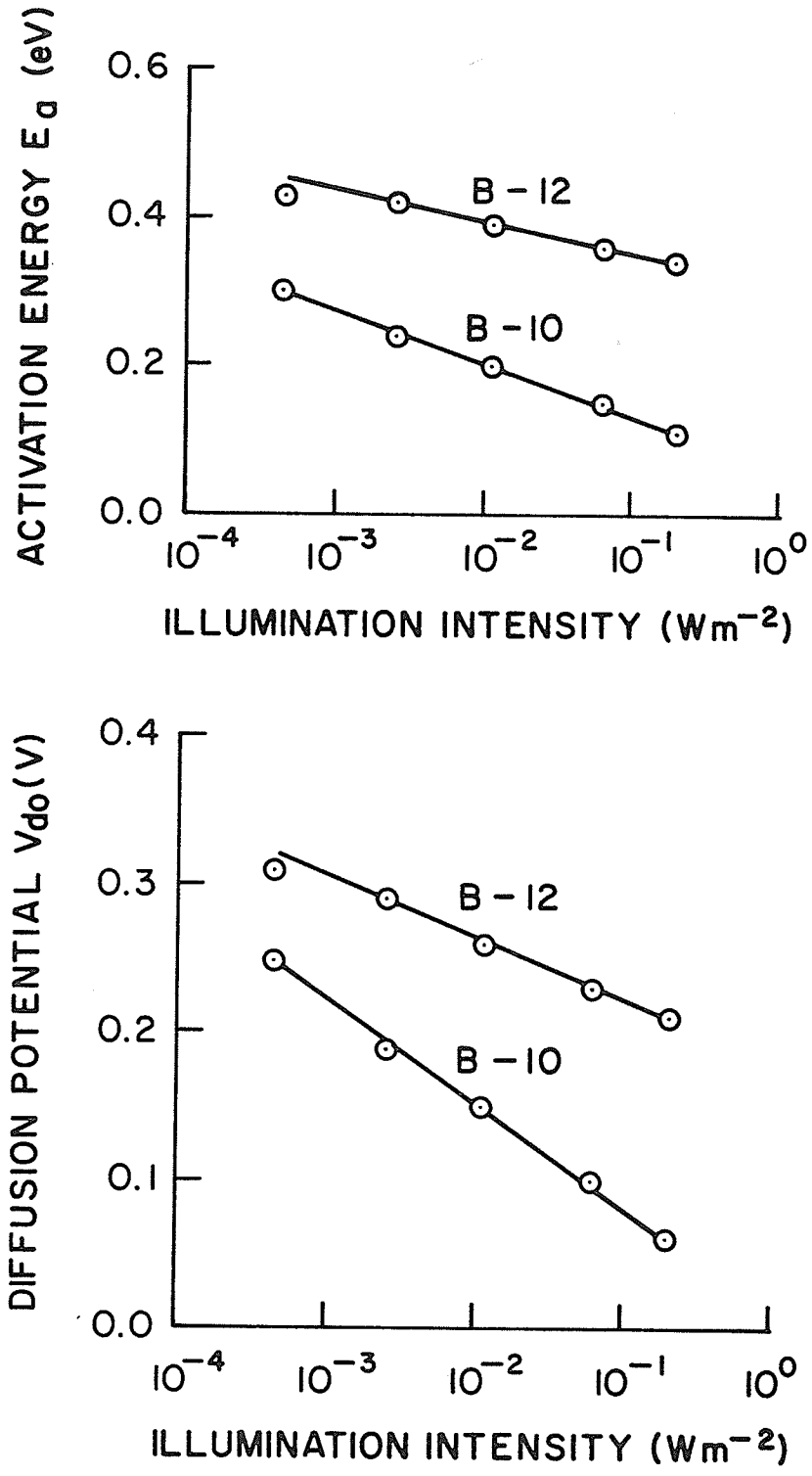

Fig. 2.9 The dependence of (a) the activation energy and (b) the diffusion potential on illumination intensity for B-10 and B 12. T = 300 K .

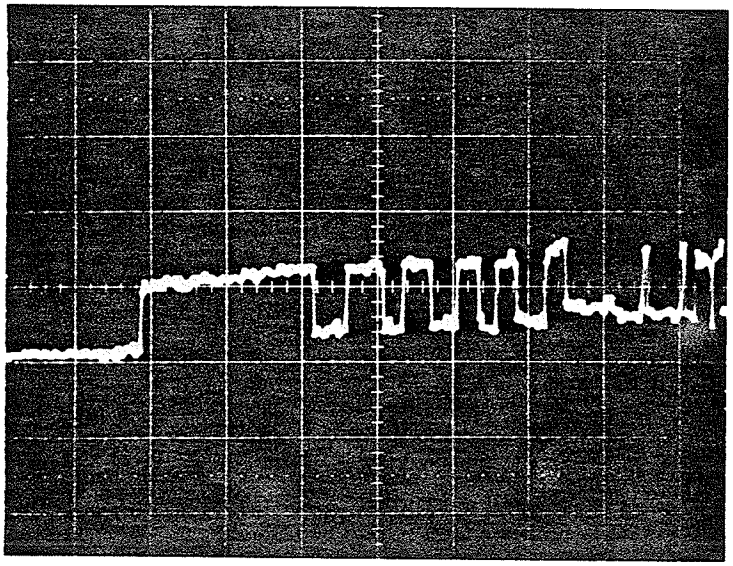

Fig. 2.10 Current oscillations observed at high d.c. current densities Grain boundary sample B-11. V = 15V, I = 150 mA. Vert. scale: 500 μA/division. Horz. scale: 1 ms/division.

The steady-state current-voltage characteristics of the grain boundary in general consist of a component due to the transport of majority carriers over the grain-boundary potential barrier, J_1, a component due to minority carriers transported in the opposite direction, J_2, and finally a component associated with recombination of electrons and holes in grain-boundary interface states, J_3. These three components are illustrated in the energy-band diagram of Fig. 2.11. Our interpretation of results such as those presented in Sec. 2.3 is that the first component is completely dominant over the other two, at least under dark conditions. This is discussed in ref. (13). That is, currents such as those of Figs. 2.2 to 2.4 are to be identified as the transport of majority carriers (in our case, holes) over the potential barrier at the grain boundary. (The downward bending of the bands at the grain boundary presents a barrier to holes.) In this interpretation we are in agreement with previous workers[4,7,10-12,16-18]. We do, however, consider the other two components in their indirect effects upon the majority-carrier current. This will be discussed further below.

The majority-carrier (hole) current is given by[13]

$$J \simeq J_1 = \frac{q N_v v_r}{1 + \frac{v_r}{v_d}} \exp(-\frac{\phi_b}{V_T}) \exp(\frac{V_1}{V_T}) [1 - \exp(-\frac{V}{V_T})] \qquad (2.1)$$

where N_v is the effective density of states in the valence band of the silicon (10^{25} m^{-3}), v_r is the grain boundary interface 'collec-

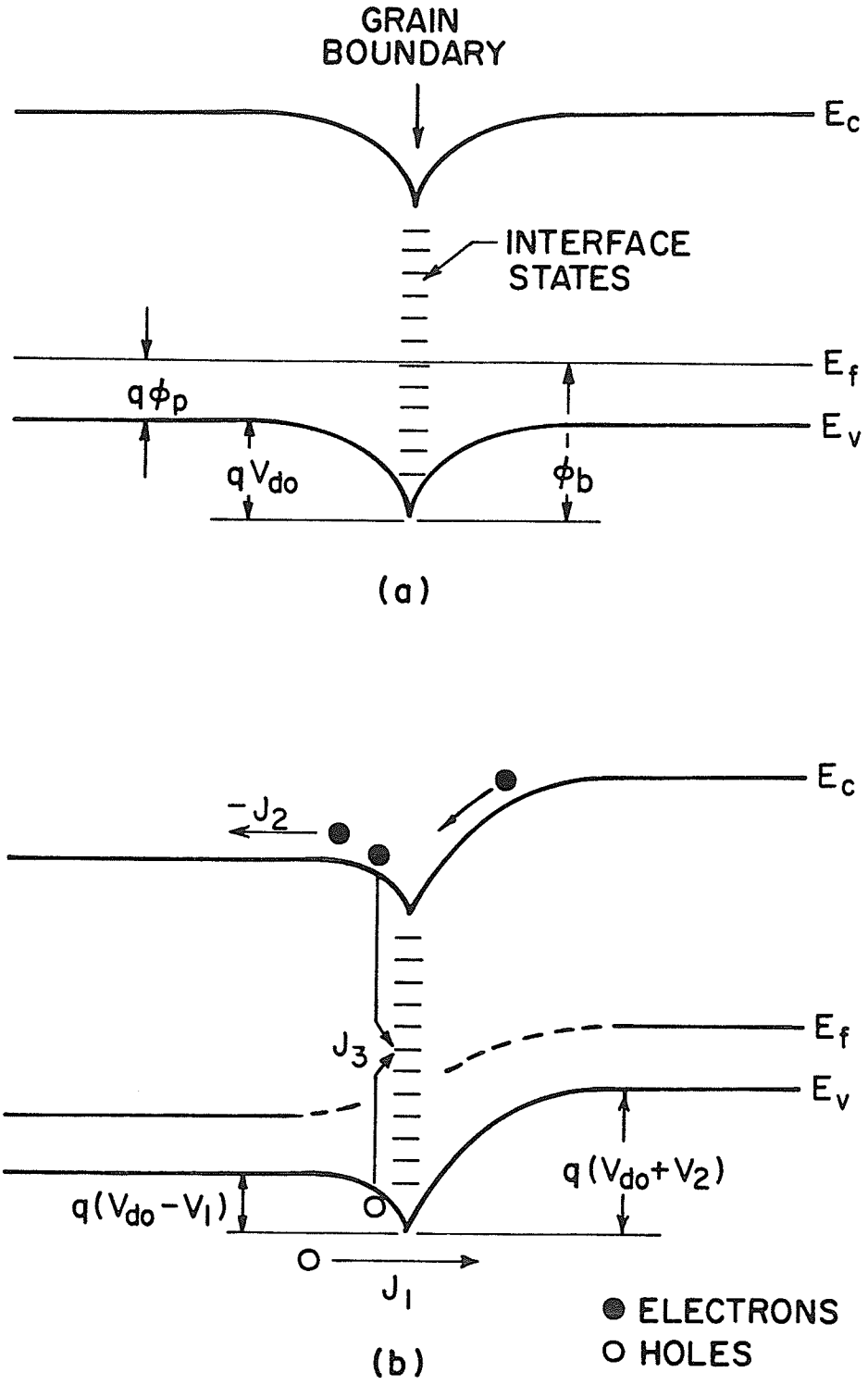

Fig. 2.11 Electron energy-band diagrams for grain boundary with (zero-bias) diffusion potential V_{do} . (a) $V = 0$; (b) $V > 0$. V_1 and V_2 are the portions of applied voltage V developed across the space-charge regions to the left and right of the grain boundary, respectively.

tion' velocity for holes, v_d is the diffusion velocity for holes in the space-charge region to the left of the grain boundary; ϕ_b is the barrier height, or the difference between the zero-bias (equilibrium) Fermi-level and the silicon valence band edge at the grain boundary; V_1 is the portion of the applied voltage V which provides a forward bias to the space-charge region on the left in Fig. 2.11 (V_2 is the reverse bias on the right-hand side of the boundary so that $V = V_1 + V_2$). $V_T = kT/q$.

Equation (2.1) is an adaptation of the treatment by Crowell and Sze[19-21] originally developed by them for Schottky barriers, i.e. for carrier transport across metal-semiconductor interfaces. In the Schottky-barrier case, v_r is usually considerably smaller than v_d, as is given in that case by $v_r = A^* T^2/q\, N_v$ where A^* is the effective Richardson constant for holes ($A^* \simeq 3 \times 10^5$ $Am^{-2} K^{-2}$ for the silicon doping concentrations encountered here).[14,15] At 300K, $A^* T^2/qN_v \simeq 2 \times 10^4$ ms^{-1} . In our grain boundary case, rather than having a metal opposite the forward-biased space-charge region as in the Schottky barrier, we have a reverse-biased space-charge region. The large electric field associated with this region is an efficient collector of majority carriers. As discussed in Part I: Theory[13], v_r in the grain boundary case is better described by $v_r \simeq v_{s\ell}$, the scattering-limited velocity for holes ($\simeq 10^5$ ms^{-1} for silicon).

The diffusion velocity $v_d \simeq \mu \xi_{m1}$, where μ is the hole mobility ($\simeq 0.05$ $m^2V^{-1}s^{-1}$ at 300K for our concentration of acceptor impurities),[14] and ξ_{m1} is the maximum electric field to the left of the grain boundary in Fig. 2.11 ($\simeq 10^6$ Vm^{-1} for $V = V_1 = 0$ and

decreasing for larger V_1). Thus $v_d \simeq 5 \times 10^4$ ms^{-1} and unlike the Schottky-barrier case v_d is somewhat less than v_r in Eqn. (2.1). Our numbers for v_r and v_d are of course approximate, but within a factor of two or so, and hence Eqn. (2.1) may be written

$$J \simeq q N_v v_d \exp(-\frac{\phi_b}{V_T}) \exp(\frac{V_1}{V_T}) [1 - \exp(-\frac{V}{V_T})]$$

$$= q N_v \mu \xi_{ml} \exp(-\frac{\phi_p}{V_T}) \exp(-\frac{V_{do}}{V_T}) \cdot$$

$$\cdot \exp(\frac{V_1}{V_T}) [1 - \exp(-\frac{V}{V_T})]$$

$$= q N_a \mu \xi_{ml} \exp(-\frac{V_{do}}{V_T}) \exp(\frac{V_1}{V_T}) [1 - \exp(-\frac{V}{V_T})] \qquad (2.2)$$

where $\phi_b = V_{do} + \phi_p$ (Fig. 2.11) and we have used $\exp(-\frac{\phi_p}{V_T}) \simeq N_a/N_v$ which is true provided the acceptor impurities (of concentration N_a) remain ionized, i.e. for $T \gtrsim 100$ K in silicon.

For $V \ll V_T$ and $V_1 \ll V_T$ we can simplify (2.2) to

$$J \simeq q N_a \mu \xi_{ml} (\frac{V}{V_T}) \exp(-\frac{V_{do}}{V_T}) \qquad (2.3a)$$

and define an activation energy for the potential barrier at the grain boundary as

$$E_a = - \frac{d \, \ell n \left(\frac{J}{qN_a \mu \xi_{ml} (V/V_T)} \right)}{d(1/T)} = \frac{q}{k} V_{do} + \frac{q}{kT} \cdot \frac{d(V_{do})}{d(1/T)}$$

$$= \frac{q}{k} \left(V_{do}(T) - T \frac{d \, V_{do}}{dT} \right) \qquad (2.4a)$$

Equations (2.3a) and (2.4a) apply for $V \ll V_T$. For relatively large applied voltages, on the other hand, i.e. for $V \gg V_T$, they are replaced by

$$J \simeq q \, N_a \, \mu \, \xi_{ml} \exp(- \frac{V_{do}}{V_T}) \exp(\frac{V_1}{V_T})$$

$$= q \, N_a \, \mu \, \xi_{ml} \exp(- \frac{V_d}{V_T}) \qquad (2.3b)$$

where $V_d = V_{do} - V_1$, and

$$E_a = - \frac{d \ln\left(\frac{J}{q N_a \mu \xi_{ml}}\right)}{d(1/T)}$$

$$= \frac{q}{k} (V_{do} - V_l) + \frac{q}{kT} \frac{d(V_{do} - V_l)}{d(1/T)}$$

$$= \frac{q}{k} \left(V_{do}(T) - T \frac{d V_d}{dT}\right) \quad . \tag{2.4b}$$

Note that the second term on the right-hand sides of Eqns. (2.4a) and (2.4b) are negative, as discussed below and exactly cancel the temperature dependence of the first term <u>for spatially-uniform grain boundaries</u>, so that in this case $E_a \neq E_a(T)$.

We have chosen to take the temperature dependence of the mobility given by[22]

$$\mu(T) = 54.3\ T_n^{-0.57} + \frac{1.36 \times 10^8\ T^{-2.23}}{1 + \left[N_a/(2.35 \times 10^{17} T_n^{2.4})\right] 0.88\ T_n^{-0.146}} \tag{2.5}$$

($T_n = T/300$) to the left hand side in Eqns. (2.4a) and (2.4b). In these equations, the parameters J , μ , and V_{do} are temperature dependent, in addition to the explicit appearance of T and $V_T = kT/q$.

The equilibrium diffusion potential V_{do} in Eqn. (2.4) is temperature-dependent for two reasons. First, the temperature depen-

dence of the bulk Fermi potential ϕ_p, given by

$$\phi_p = \frac{kT}{q} \ell n \, (N_v/N_a) \tag{2.6}$$

gives rise to a temperature dependence of V_{do} which may be written as

$$\frac{d\, V_{do}}{dT} = -\gamma \frac{d\, \phi_p}{dT}$$

$$\simeq -\frac{\gamma k}{q} \ell n \, (N_v/N_a) \tag{2.7}$$

where we have used Eqn. (2.6) and neglected the weak temperature dependence of $\ell n \, N_v$. γ is a parameter which accounts for Fermi-level pinning at the grain boundary by interface states. For samples B-12 and B-10 for example, we have that $\gamma \simeq 1.0$ and $\gamma \simeq 0.6$ respectively, for the N_{is} measured in these samples [see Appendix for derivation of γ].

Second, the occurrence of a spatial variation of diffusion potential over the grain-boundary plane will give rise to an 'effective V_{do}' in Eqn. (2.3) which also exhibits a temperature dependence in addition to that of Eqn. (2.7). This is because the current transport through various portions of the grain boundary with different V_{do} will be weighted by the temperature-dependent factor $\exp(-qV_{do}/kT)$. At lower temperatures a larger portion of the current will flow through the regions of lowest V_{do} and the effective V_{do} will decrease. For

a spatially uniform grain boundary $d V_{do}/dT$ is therefore given by Eqn. (2.7), whereas for a nonuniform boundary, an additional term dependent upon the nature of the spatial nonuniformity contributes to $\frac{d V_{do}}{dT}$.

The maximum electric field ξ_{m1} in Eqn. (2.3) corresponds to that close to the grain boundary on the left-hand side of Fig. 2.11, given in the depletion approximation by[23]

$$\xi_{m1} \simeq \left[\frac{2qN_a}{\varepsilon_s} (V_{do} - V_1 - V_T) \right]^{1/2} \tag{2.8}$$

where ε_s is the permittivity of silicon.

As the applied voltage V increases, we have that

$$V = V_1 + V_2 \tag{2.9}$$

$$\begin{aligned} Q_1 &= -q N_a W_1 \\ &= -\left[2q \varepsilon_s N_a (V_{do} - V_1 - V_T)\right]^{1/2} \end{aligned} \tag{2.10}$$

$$\begin{aligned} Q_2 &= -q N_a W_2 \\ &= -\left[2q \varepsilon_s N_a (V_{do} + V_2 - V_T)\right]^{1/2} \end{aligned} \tag{2.11}$$

and

$$Q_1 + Q_2 + Q_{is} = 0 \qquad (2.12)$$

for all V. V_{do}, V_1 and V_2 have been defined above; W_1 and W_2 are the widths of the space-charge regions on the forward and reverse-biased sides of the grain boundary, respectively. Q_1 and Q_2 are the charge (per unit area) in these space-charge regions (within the depletion approximation), and Q_{is} is the charge per unit area in the grain-boundary interface states.

Let us assume that the grain-boundary interface states remain in equilibrium with the majority carriers (holes) under an applied bias voltage. If we adopt the convention of earlier workers[11,12] that the majority carrier transport can be approximated by the emission model then the quasi-Fermi level for holes at the grain-boundary interface is approximately equal to its value in the bulk on the forward-biased side[21]. From this it follows that

$$Q_{is}(V) = Q_{is}(0) + q\, N_{is}\, V_1 \qquad (2.13)$$

for an interface-state density $N_{is}(m^{-2}\ eV^{-1})$ which is independent of energy. For an energy-dependent interface-state density, $N_{is}V_1$ in Eqn. (2.13) must be replaced by $\int N_{is}\, dV_1$.

It is important to realize that the value of N_{is} deduced from measurements using Eqn. (2.13) represents a <u>lower limit</u> on the true interface-state density. From the discussion of the majority-carrier transport above and in the Shaw and Card paper[13] we

anticipate a hole transport which is restricted by the supply of holes to the grain boundary (emission/diffusion model) and an appreciable change in the hole quasi-Fermi level E_{fp} across the forward-biased space-charge region. Thus the change in E_{fp} at the grain boundary with applied voltage will be somewhat less than V_1 and N_{is} will be underestimated using Eqn. (2.13) with the experimentally-determined $Q_{is}(V)$.

Finally, we point out that the grain boundaries were modeled as planar interfaces; the possibility of curvature on a macroscopic scale was not accounted for. This may affect the numerical values of N_{is} to some degree.

2.5 Discussion of Results

We have used the transport model of Section 2.4 to analyze the results of Figs. 2.2-2.9. This treatment assumes a grain boundary potential which is spatially uniform over the boundary plane, in accordance with the treatment in the Shaw and Card paper.[13]

As a general interpretation of the current-voltage characteristics of Figs. 2.2-2.4, at very low voltages ($V < V_T$) the curves are near ohmic as expected from Eqn. (2.3) as well as the computations in Part I: Theory. At higher voltages, the increase in J with V originates primarily from the $\exp(V_1/V_T)$ term in Eqn. (2.2). The detailed shape of the characteristic depends upon the variation of V_1 with V , which in turn is controlled by the degree of pinning of the quasi-Fermi level for holes by grain-boundary interface states. The concave nature of these curves at higher V is associated with a high

density of interface states N_{is} near midgap (strong pinning), which drops off appreciably towards the valence band. This interpretation is consistent with that offered by Seager et al[10-12] for grain boundaries in n-type silicon, in which case N_{is} also falls towards the conduction band.

N_{is} is an important parameter since, among other things, this determines the appropriate value of γ to be used in Eqn. (2.7). We have determined N_{is} as a function of energy by analysis of the current-voltage characteristics at a constant temperature, (Fig. 2.2) in terms of the emission/diffusion theory of the carrier transport. This is in the spirit of the deconvolution scheme of Seager et al[10-12], and data at three measurement temperatures have been combined to give rise to the N_{is} vs E of Fig. 2.12. For this sample γ is then determined to be 0.6, as described in the appendix. Our results for N_{is} agree within an order of magnitude with those obtained by Seager et al[10-12], in their case in the upper half of the bandgap in neutron-transmutation doped silicon. Comparison of $N_{is}(E)$ with earlier workers is made in Fig. 2.13. The picture which emerges is a peak in the density of interface states of magnitude $N_{is} \simeq 10^{16}\ m^{-2}\ eV^{-1}$ or greater and of energy spread $\Delta E \simeq 0.1$ eV. This pronounced non-uniformity in the energy distribution of N_{is} is not included in the computations of Part I, which explains the reduced structure in the calculated current-voltage characteristics.

In Fig. 2.7, we show the dependence of the activation energy E_a (defined in Eqn. 2.4b) upon the voltage applied to the grain boundary. In the determination of E_a, the temperature dependence of

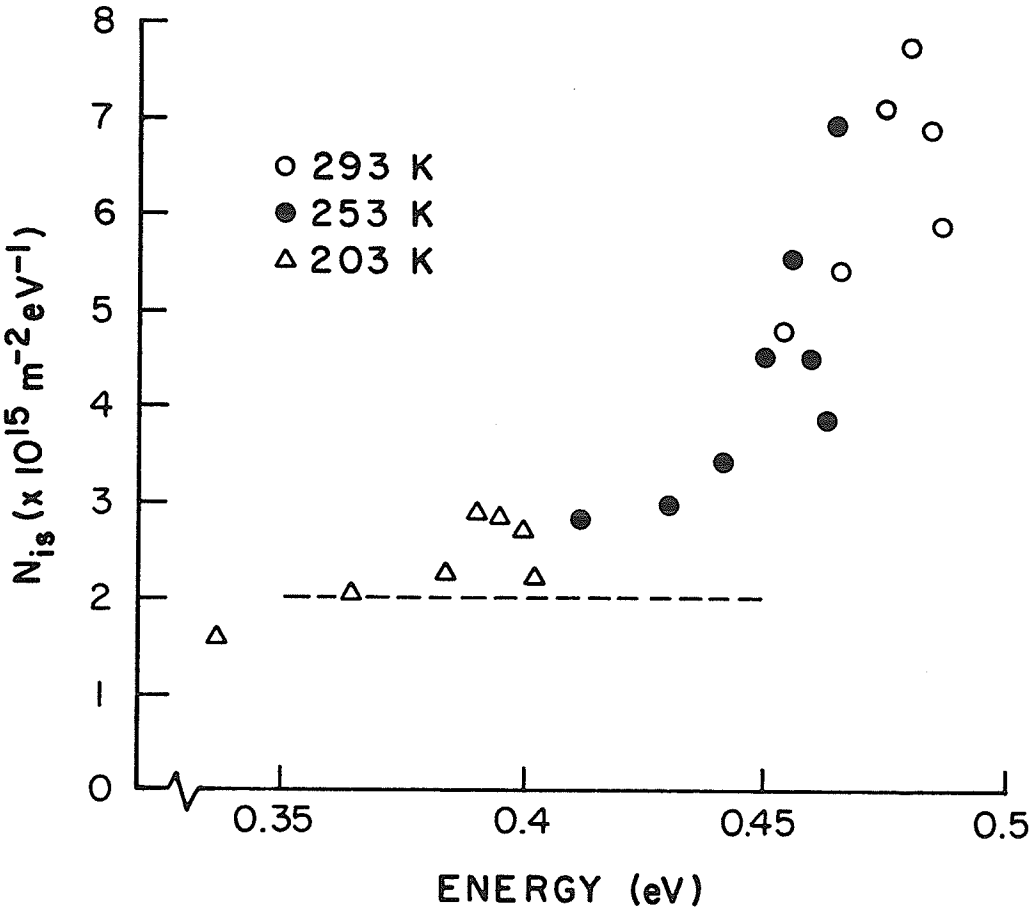

Fig. 2.12 Density of localized grain boundary interface states vs. energy in band gap of silicon (sample B-10). Points show results obtained from current-voltage characteristics at constant temperature T , for three values of T .

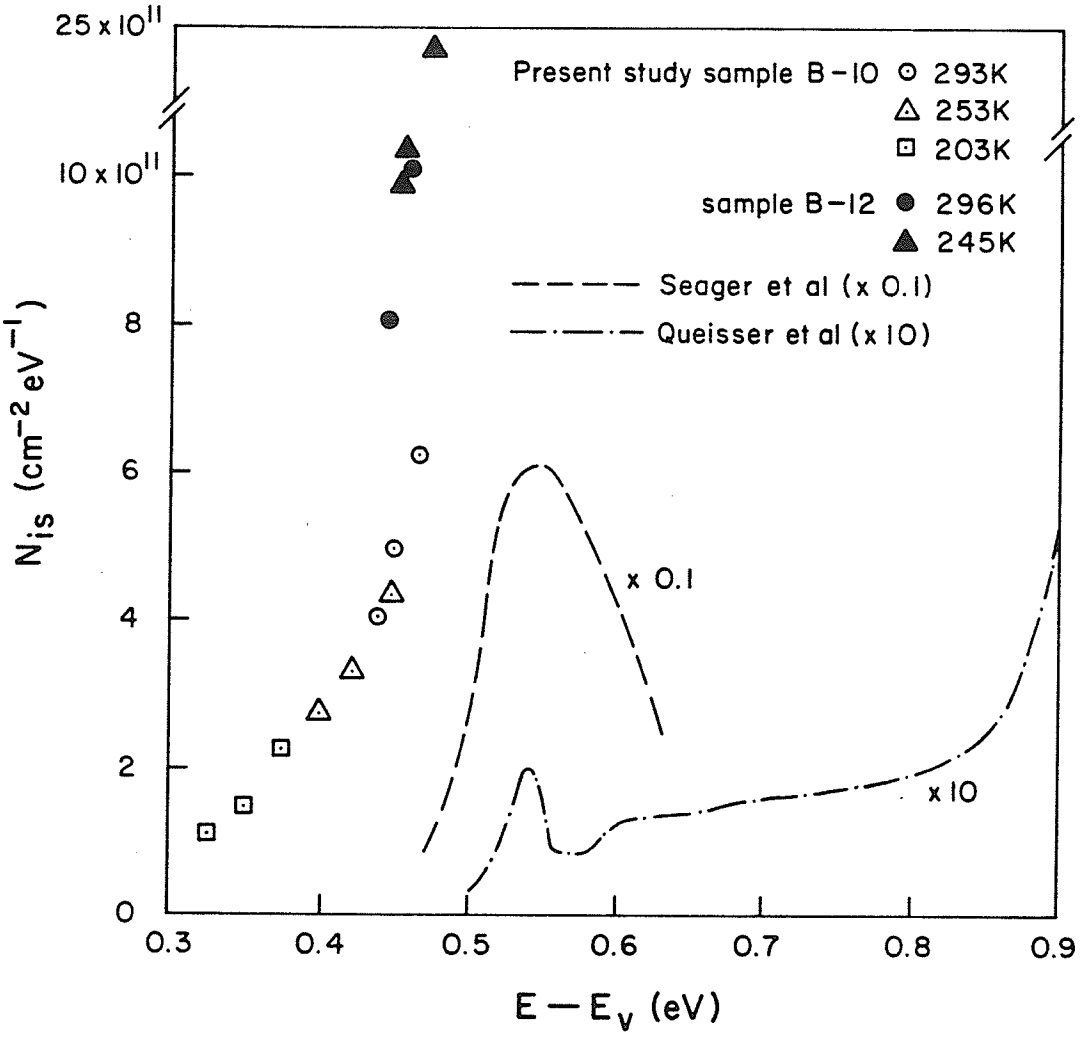

Fig. 2.13 Comparison of present results for grain-boundary interface states with earlier results for silicon grain boundaries (Refs. 26 and 27). Note units of N_{is} are $cm^{-2}eV^{-1}$ for this figure.

the mobility, given by Eqn. (2.5), has been removed, i.e. $\ell n\ (J/qN_a\mu(T)\xi_{ml})$ is plotted vs $1/T$, and the slope used to find E_a in accordance with Eqn. (2.4b). For grain boundaries which are spatially uniform, we can interpret the decrease in E_a at the larger V unambiguously as arising from a decrease in diffusion potential $V_d = V_{do} - V_1$ due to the increase in V_1 (see Eqn. (2.4b)). As we see below this is the case for grain boundary sample B-12 but not for B-10 or B-6.

One should realize that the considerably smaller value of E_a for sample B-6 as compared to B-10 and B-12 is a property of the temperature dependence of the current. This does not imply that the absolute value of the current density at a given temperature is much larger. The value of the current density is controlled by the diffusion potential V_{do}, which for sample B-6 is not significantly lower than for the other samples. The relation between V_{do} and E_a is strongly dependent on the nonuniformity of the grain boundary.

The increase in E_a with V for B-12, which appears in Fig. 2.7, can be explained by a detailed analysis of the variation in the pre-exponential term of Eqn. (2.1) with field and temperature. The fundamental reason for the increase in E_a is that the increase in the magnitude of the pre-exponential term with applied voltage is swifter at higher temperatures yielding an activation energy that increases with applied voltage. A more detailed explanation is given in Appendix C.

In the case of grain boundaries B-6 and B-10, arguments which follow indicate that these samples exhibit substantial nonuniformity in their diffusion potentials over the plane of the grain boundary. This

prohibits the analysis of the results of Fig. 2.7 for B-6 and B-10 in terms of the model of Section 2.4, which presupposes spatially uniform grain-boundary potentials.

In Fig. 2.8 we show how E_a and V_{do} depend upon temperature for the two grain boundaries B-10 and B-12. For a uniform grain boundary, the activation energy E_a will be equal to V_{do} for very small $N_{is}(\gamma = 0)$ and to ϕ_b in Fig. 2.11 for very large $N_{is}(\gamma = 1)$. It must be stressed that, in order to recover the equilibrium diffusion potential V_{do} from the activation energy E_a, we must employ the analysis of Sec. 4 and in particular Eqn. (2.4a), since $V < V_T$ in the experimental determination of E_a. Knowing the γ to be used in (7), we obtain dV_{do}/dT for Eqn. (4a) which allows us to determine V_{do} from E_a. We have therefore implicitly assumed grain boundaries which are <u>spatially uniform</u> in their properties. In Fig. 2.8(b) we show the results of this procedure for B-10 and B-12, together with the dependence of V_{do} upon T expected theoretically. As we readily observe, B-12 conforms well to the uniform model of Sec. 4 with a V_{do} which decreases slightly with T, in accordance with the temperature dependence of the bulk Fermi potential ϕ_p.

On the other hand, as was discussed in the paragraph following Eqn. (2.7), a grain boundary with spatially nonuniform properties may show a marked <u>increase</u> of E_a and V_{do} with T. This is the case for sample B-10 in Fig. 2.8. We conclude that while B-12 represents a uniform grain boundary which is fair game for the model of Sec. 4, and which therefore allows an accurate quantitative determination of $V_{do}(T)$ as in Fig. 2.8(b), sample B-10 does not. The data of Fig.

2.8(b) are not expected to be quantitatively correct for B-10, and the most we can say is qualitatively that V_{do} increases substantially with increasing temperature as a consequence of its spatially nonuniform grain boundary potential. Even if Eqn. (2.3a) applies with an "effective" $V_{do}(T)$, the unknown form of the temperature dependence excludes a separation of the two terms on the right hand side of Eqn. (2.4a) for nonuniform samples. We have separately obtained a first-order model for B-10 by assuming a gaussian distribution of V_{do} values over the grain-boundary plane, this work will be presented in Chapter III.

The origin of the nonuniformity in diffusion potential for B-10 (also B-6 and others, not shown) is thought to be a spatial variation over the plane of the grain boundary in N_{is}, in N_a, or both. This nonuniformity must be over macroscopic distances (greater than the width W_1, W_2 of the space-charge regions) since otherwise their effects would be integrated electrostatically. The segregation of dopant impurities to the grain boundary can also affect the interface-state distribution in a spatially nonuniform way. We must point out that in the work of Seager et al[10-12,14], the impurities were introduced by neutron-transmutation doping, which is expected to produce a uniform N_a, unlike the present case of cast silicon with dopant introduced into the melt.[24] At any rate, it seems fairly certain that both uniform and nonuniform grain boundaries exist in the Wacker silicon material of this study.

One possible source of spatial nonuniformity is the surface region of the sample. We are satisfied that this is not important in

our samples on the basis of experiments with a zerostat, which allows us to deposit either positive or negative charge on the surface.[25] The deposition of negative charge causes a noticeable temporary increase in the current across the grain boundary, undoubtedly because the potential barrier of this boundary is substantially lowered near the surface by the negative charge. On the other hand, the deposition of positive charge on the surface of a virgin sample has no observable effect, which implies that the grain-boundary barrier near the surface of an undisturbed sample is not substantially lower than in the bulk. The barrier near the surface may instead be higher, of course, but the fraction of the total current-carrying area affected is small enough to be neglected in this case.

It is observed in Figs. 2.5 and 2.6, and also in Fig. 2.9, that the exposure of the samples to optical illumination substantially reduces the diffusion potential at the grain boundary. Comparing B-6 and B-10 in Fig. 2.6 shows that the grain boundary with the larger V_{do} (B-10) exhibits a much greater sensitivity to illumination. These effects were predicted earlier[8] and may be understood by considering the effects of photogenerated minority carriers (electrons) which are attracted to the grain boundary by the electric field in the adjacent space-charge regions. Electrons accumulate at the grain boundary until their concentration reaches the magnitude at which their capture by the interface states exactly balances the supply by photogeneration within a diffusion length on either side of the grain boundary. Provided this electron concentration (which increases approximately linearly with photogeneration rate) is sufficiently large that $n \sigma_n \simeq p \sigma_p$ (σ_n ,

σ_p are the capture cross-sections of grain-boundary interface states for electrons and holes) the interface charge Q_{is} will decrease.[26] More interface states will be occupied by electrons than under dark conditions, and V_d will decrease below its dark value V_{do}. The effect is reduced in B-6 because the lower V_{do} implies a larger p, which requires a larger n (higher optical intensity) to meet the $n\sigma_n \simeq p\sigma_p$ condition.

The results of Fig. 2.9 further indicate that, for each order of magnitude change in the photogeneration rate, the value of V_d for $V = 0$ decreases by approximately 0.07 eV. Since the majority carrier concentration at the grain boundary $p \sim \exp(-V_d/V_T)$ and $V_T = 0.026$ V at 300K, we expect approximately an order of magnitude increase in this concentration. This observation is consistent with our earlier theoretical work, and confirms that for appreciable photogeneration, $n\sigma_n \approx p\sigma_p$ at the grain boundary.[8] This condition implies a charge in grain boundary interface-states which is modified by the photogeneration in such a way that the decrease in diffusion potential ΔV_d is one half of the quasi-Fermi level separation $\Delta E_F = E_{fn} - E_{fp}$ at the grain boundary.[17]

Series resistance effects from the bulk silicon grains has been found to be negligible in the data presented in Sec. 3, except at the largest current densities and lowest V_{do}. For these currents, the coalescence of the various curves at different temperature and optical illumination intensities (Figs. 2.2 to 2.5) indicate the onset of series resistance effects. For the nonuniform grain boundaries,

this mechanism occurs at lower current densities than would be expected on the basis of a one-dimensional model of current transport, particularly at low temperatures. This is understandable since at the low temperature, the effective area of active grain boundary conduction is small and under these conditions, the series resistance increases and is explained in terms of a spreading resistance calculation.

Additional support for the notion of characteristic interface defects (a peak in N_{is} near midgap) comes from a consideration of the crystal mismatch at the grain boundary. Let us consider this mismatch on the basis of a simple model such as that of Fig. 2.14. This represents a realistic mismatch angle for grain boundaries in cast silicon. Note that characteristic defects are periodically repeated along the grain boundary plane but at distances of many atomic spacings. In the vertical direction, the repetition distance will be much shorter, the dimension of a unit cell. It is clear that not all of these defect sites contribute interface states near midgap (which would correspond to unsatisfied bonds) since $\int N_{is}\, dE \simeq 10^{15} - 10^{16}\ m^{-2}$ over the energy range corresponding to the midgap peak, whereas the total density of atoms on the boundary plane is $10^3 - 10^4$ times larger. This assumes that the orientational mismatch between adjacent grains is preserved over macroscopic distances.[27]

It is interesting to also note that, by virtue of the periodic nature of the defect structure, a two-dimensional band conduction should be possible in the grain-boundary plane. These bands will be rather narrow for momentum parallel to the page in Fig. 2.13 as a result of the repetition length being several atomic distances, but could be wide for transport in the perpendicular direction.

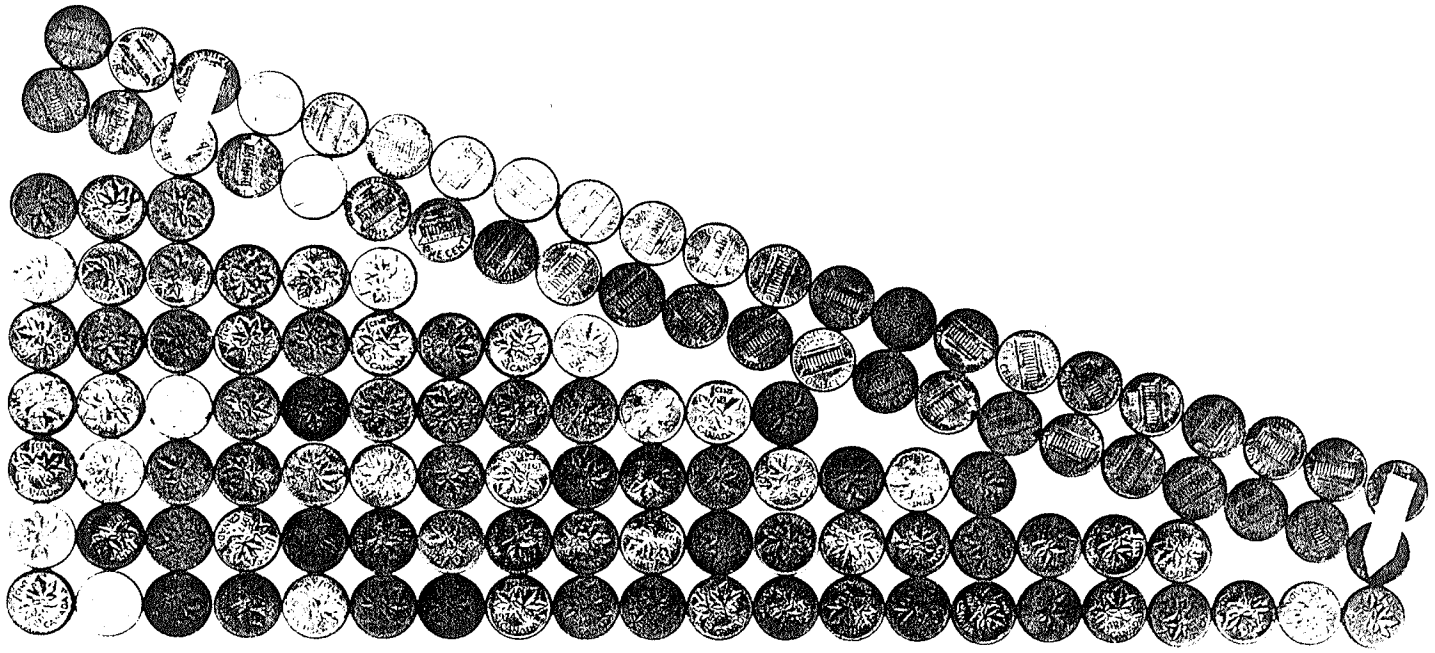

Fig. 2.14 Model of grain boundary for orientational mismatch of ≃ 20°, showing periodic nature of particular defect structure. Variety of bonding disorder is suggested over one period. Note repetition of approximately periodic disorder with a period of three atomic spacings along Canadian-American border.

With regard to the oscillations reported earlier, we believe these to be due to electric-field enhanced emission from the localized interface states at the grain boundary. The beneficial effect of increased temperature supports this view, as it would provide for thermally-assisted field emission. An alternative explanation which we considered for a time was impact ionization in the localized regions of high electric field that are expected from the spatial non-uniformity of the grain-boundary potentials, but this would be expected to display a negative temperature coefficient.

The relative orientations of the crystals on either side of the interface of sample (B-10) of Figs. 2.2,2.5, and 2.7-2.9 were measured using x-ray precession photography.[28] The crystals were found to have a 9° mismatch of the (111) planes. Moreover the grain-boundary plane bisected this mismatch angle. More details of this technique will be reported in Chapter IV.

2.6 Conclusions

On the basis of the experimental studies described in this chapter, and the theoretical arguments concerning the collection velocity for majority carriers of the grain boundary, the rate-limiting process of majority carrier supply by diffusion to the grain boundary should be incorporated into the transport model. The thermionic emission theory used by previous authors is expected to provide at best an order of magnitude estimate of the current across the electrically-biased grain boundary. Grain boundaries with a variety of diffusion potentials exist[29] in Wacker 'Silso' silicon, and many of these bound-

aries contain potential barriers which are spatially nonuniform over macroscopic portions of the grain-boundary plane. Spatially-uniform grain boundaries also exist in this material, and for these samples a reasonable agreement with the theoretical predictions of Shaw and Card[13] is obtained. Departures from the predicted characteristics may be accounted for by the overly-restrictive assumption made there of an energy-independent interface-state density. Grain boundary interface-state densitites measured in this material are in the range of 10^{15} to 10^{16} m^{-2} eV^{-1} and exhibit an increase with energy away from E_v in the lower half of the energy gap between 0.3 and 0.5 eV. More direct measurements of these interface-state distributions, such as depleted-layer spectroscopy techniques[30] are necessary for accurate determinations, since the results are otherwise transport model dependent. An adequate understanding of grain boundary phenomena in cast silicon materials, or vapor-deposited polycrystalline thin films, will challenge research workers for some time to come.

CHAPTER III

Effects of Interface-Potential Nonuniformities on Carrier Transport across Silicon Grain Boundaries*

3.1 Introduction and Theory

In the previous chapter it was shown that the experimental activation energy for majority carrier transport across particular isolated grain boundaries decreased rapidly with decreasing temperature. This effect was attributed to the increasing sensitivity of the boundary to variations in diffusion potential V_d as the temperature was lowered, in accordance with a thermally-activated ($\exp(-q\ V_d/kT)$) process.

In the previous chapter[13] a new model was presented for the majority-carrier transport process, but non-uniform conduction through grain boundaries was not treated quantitatively. The model is an extension of an earlier formulation for current flow in Schottky barriers developed by Crowell and Sze.[36] As shown in Chapter II, the majority-carrier (in our case, hole) current is given by [33]

$$J = \frac{q\ N_v\ V_r}{1 + \frac{V_r}{V_d}} \exp\left(\frac{-\phi_b}{V_T}\right)\exp\left(\frac{V_1}{V_T}\right)\left[1 - \exp\left(\frac{-V}{V_T}\right)\right] \qquad (3.1)$$

---

*The contents of this chapter have been submitted for publication to the Journal of Applied Physics, October 1982.

where N_v is the effective density of states in the valence band of the silicon, V_r is the grain-boundary interface "collection" velocity for holes, V_d is the diffusion velocity for holes in the space-charge region adjacent to the grain-boundary; ϕ_b is the barrier height, or the difference between the zero-bias (equilibrium) Fermi-level and the silicon valence-band edge at the grain boundary, V_1 is the portion of the applied voltage V which is developed across the forward-biased side of the boundary and $V_T = kT/q$; these parameters are shown in Fig. 3.1.

Using Eqn. (1) the argument was presented that the collection velocity of the boundary would not be $V_r = A^*T^2/q\,N_v$ as in a Schottky barrier where A^* is the effective Richardson constant, but rather the collection velocity of a reverse-biased space-charge region, $V_r = \mu\,\varepsilon_{max}$, where ε_{max} is the maximum electric field, i.e. the field very close to the boundary interface. Since the diffusion velocity is also $V_d = \mu_{max}$ the current density can be simplified, for the case of low bias voltage, to

$$J = \frac{q\,N_v\,\mu\,\varepsilon_{max}}{2}\exp\left(\frac{-\phi_b}{V_T}\right)\exp\left(\frac{V_1}{V_T}\right)\left[1 - \exp\left(\frac{-V}{V_T}\right)\right] \qquad (3.2)$$

Using the substitutions $\phi_b = V_{do} + \phi_p$ and $\exp(-\phi_p/V_T) \simeq N_a/N_v$ the formula (3.2) may be rewritten as

$$J \simeq \frac{q\,\mu\,\varepsilon_{max}\,N_a}{2}\exp\left(\frac{-V_{do}}{V_T}\right)\exp\left(\frac{V_1}{V_T}\right)\left[1 - \exp\left(\frac{-V}{V_T}\right)\right] \qquad (3.3)$$

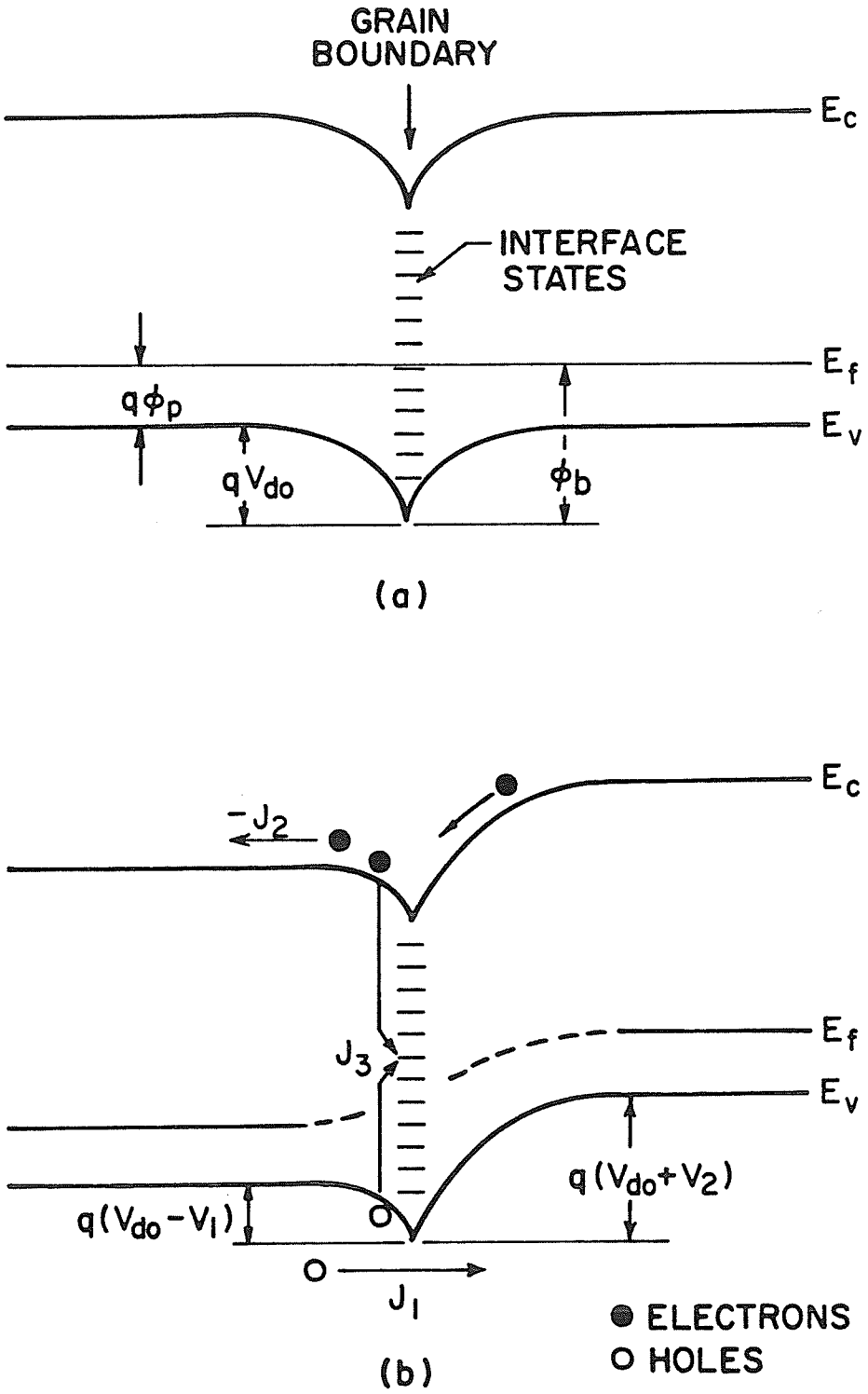

Fig. 3.1 Band diagram of grain boundary with and without bias.

For the case $V_1 < V_T$ Eqn. (3.3) may be approximated by

$$J \simeq \frac{q \mu \varepsilon_{max} N_a}{2} \frac{V}{V_T} \exp(\frac{-V_{do}}{V_T}) \qquad (3.4)$$

Eqn. (3.4) applies to transport of majority carriers across a grain boundary with spatially uniform properties; let us now apply this model to the analysis of a nonuniform boundary.

To find the total current across a nonuniform boundary we make use of an expression similar to Eqn. (3.4). However, in the case of a nonuniform boundary $\exp[-\frac{V_{do}}{V_T}]$ must be replaced by an integral of the form

$$\exp(-\frac{V_{do}}{V_T}) = \int_0^\infty a(V_d)\exp(-\frac{V_d}{V_T})\, dV_d \qquad (3.5)$$

where $a(V_d)\, dV_d$ gives the incremental area of the boundary with diffusion potential V_d, $a(V_d)$ is normalized to unit area and $\exp(-\frac{V_d}{V_T})$ is the exponential weighting factor. Areas of lower V_d will carry higher current densities. To evaluate (3.5) we must first assume an appropriate distribution of areas $a(V_d)$. Since the boundaries studied were believed to contain defects of a random nature[33] an appropriate first choice of $a(V_d)$ is a gaussian distribution, that is

$$a(V_d) = \frac{1}{\sqrt{2\pi}\,\sigma} \exp\left[- \frac{(V_d - \langle V_d \rangle)^2}{2\sigma^2} \right] \qquad (3.6)$$

where σ is the standard deviation of the diffusion potential over the grain boundary plane and $\langle V_d \rangle$ is the mean value. A typical plot of $a(V_d)$ vs V_d is shown in Fig. 3.2 ($\langle V_d \rangle = 0.50$, $\sigma = 0.08$). If (3.6) is substituted into (3.5) the integral can be evaluated and a solution for J may be obtained. However, let us first examine the kernel of (3.5) with the substitution of Eqn. (3.6). If we plot $a(V_d) \exp(-\frac{V_d}{V_T})$ vs V_d for two temperatures, as in Fig. 3.3, we note two observations; (1) at higher temperatures the area under the graph is larger and therefore the current is also larger, and (2) the peak in the graph shifts to lower values of V_d, that is the current tends to be transmitted through those areas having lower V_d, at the lower temperatures.

Now that we have examined the kernel of the integral in (3.5) for its basic properties, let us evaluate this expression. Using standard integration tables[34] we find that Eqn. (3.5) with the substitution of (3.6) is given by, (the details of this calculation are given in Appendix B)

$$\exp\left[- \frac{V_{do}}{V_T} \right] = \frac{1}{2} \exp\left[- \frac{\langle V_d \rangle}{V_T} + \frac{\sigma^2}{2V_T^2} \right] \operatorname{erfc}\left[\frac{\frac{\sigma}{V_T} - \frac{\langle V_d \rangle}{\sigma}}{\sqrt{2}} \right] \qquad (3.7)$$

The erfc [•••] term in expression (3.7) results from the integration corresponding to $0 < V_d < \infty$ rather than $-\infty < V_d < \infty$. The erfc [•••] also sets a limit on the expression because if $\frac{\sigma}{V_T} > \frac{\langle V_d \rangle}{\sigma}$

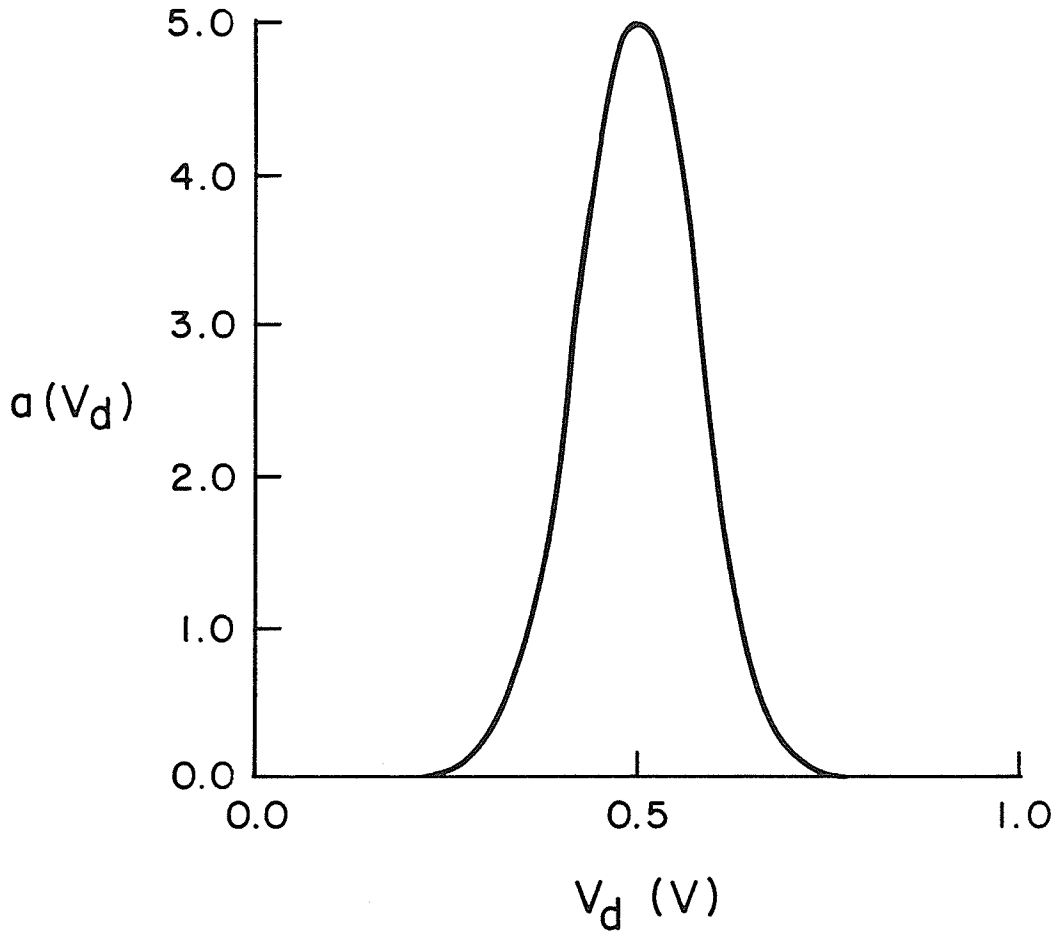

Fig. 3.2 Plot of $a(V_d)$ vs V_d for $\langle V_d \rangle = 0.50$ and $\sigma = 0.08$.

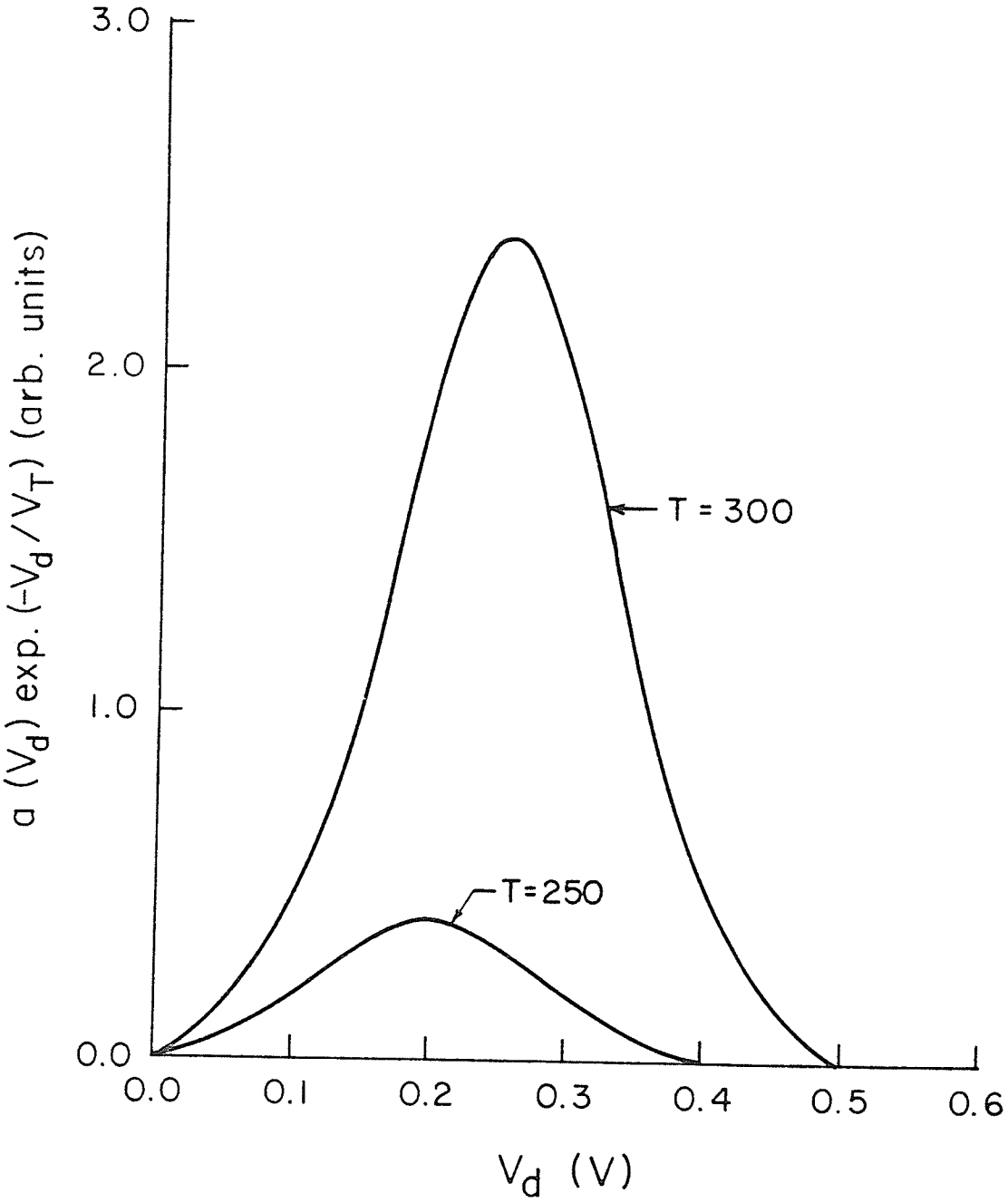

Fig. 3.3 Plot of the kernel of integral (5) for T = 300K and T = 250K with $\langle V_d \rangle = 0.50$ and $\sigma = 0.08$.

the kernel has a significant value at $V_d < 0$ and the model becomes invalid. However in the cases studied $\frac{\sigma}{V_T} < \frac{\langle V_d \rangle}{\sigma}$ and we may use the approximation that

$$\operatorname{erfc}\left[\frac{\frac{\sigma}{V_T} - \frac{\langle V_d \rangle}{\sigma}}{\sqrt{2}} \right] \simeq 2 \qquad (3.8)$$

Substituting (3.8) into (3.7) yields

$$\exp\left[\frac{-V_{do}}{V_T} \right] = \exp\left[\frac{-\langle V_d \rangle}{V_T} + \frac{\sigma^2}{2 V_T^2} \right] \qquad (3.9)$$

In examining (3.9) one can see that in the limit as $\sigma \to 0$ (3.9) will reduce to the case of a uniform boundary. Equation (3.9) can also be used to solve for V_{do}

$$V_{do} = \langle V_d \rangle - \frac{\sigma^2}{2 V_T} \qquad (3.10)$$

Equation (3.10) implies that a nonuniform boundary of this type can be regarded as having a temperature-dependent value of the equilibrium diffusion potential V_{do} through the $V_T = kT/q$ factor in Eqn. (3.10), and a temperature-independent area for current flow.

An equation such as (3.10) does not contain all of the temperature dependence of the conductance. One must also consider the shift in the bulk Fermi-level with temperature. Since the bulk Fermi potential $\phi_p \simeq kT \ell n(N_v/N_a)$, we can write

$$\frac{d\phi_p}{dT} \simeq k \ell n(N_v/N_a) \tag{3.11}$$

which is approximately independent of T (N_v is only weakly temperature dependent). The shift in the Fermi potential and hence in V_d at the grain boundary due to this bulk shift may be represented by

$$\Delta V_d = \gamma \Delta T \frac{d\phi_p}{dT} \tag{3.12}$$

where γ is a constant dependent upon the density of interface states at the grain boundary[1] and ΔT is the temperature excursion.

If Eqns. (3.9) and (3.12) are now used in (3.4), the current density is given by

$$J \simeq \frac{q \mu_{max} N_a}{2} \frac{V}{V_T} \exp\left[- \frac{\langle V_d \rangle}{V_T} + \frac{\sigma^2}{2V_T^2} - \frac{\gamma \Delta T \frac{d\phi_p}{dT}}{V_T} \right] \tag{3.13}$$

We define a thermal activation energy as

$$E_a(T) = \frac{d}{d(1/T)} \ell n\left[\frac{2J}{q\,\mu\,\varepsilon_{max}\,N_a} \frac{V_T}{V} \right] \qquad (3.14)$$

and apply (3.14) to (3.13) to obtain

$$E_a(T) = q\left[- < V_d > + \frac{\sigma^2}{V_T} - \gamma\, T \frac{d\,\phi_p}{dT} \right] \qquad (3.15)$$

With independent knowledge of the doping concentration N_a within the grains, the total cross-sectional area of the sample, and the interface state density (and hence γ) at the boundary we can obtain $< V_d >$ and σ from a plot of E_a vs $1/T$.

3.2 Experimental Results and Discussion

The details of sample preparation and measurement are identical to those given in Chapter 2 and are not repeated here.

The raw data for the current-voltage characteristics of two isolated grain boundaries at several measurement temperatures are shown in Fig. 3.4 and Fig. 3.5. In the analysis presented here, we employed the assumption of a sufficiently high density of interface states ($\geq 10^{12}$ cm^{-2} eV^{-1}), consistent with experimental observations of other authors,[12] to results in a $\gamma \simeq 1$ in Eqn. (3.15).[33] This implies that the entire shift with temperature of the bulk Fermi level is transferred to the diffusion potential at the grain boundary. A plot

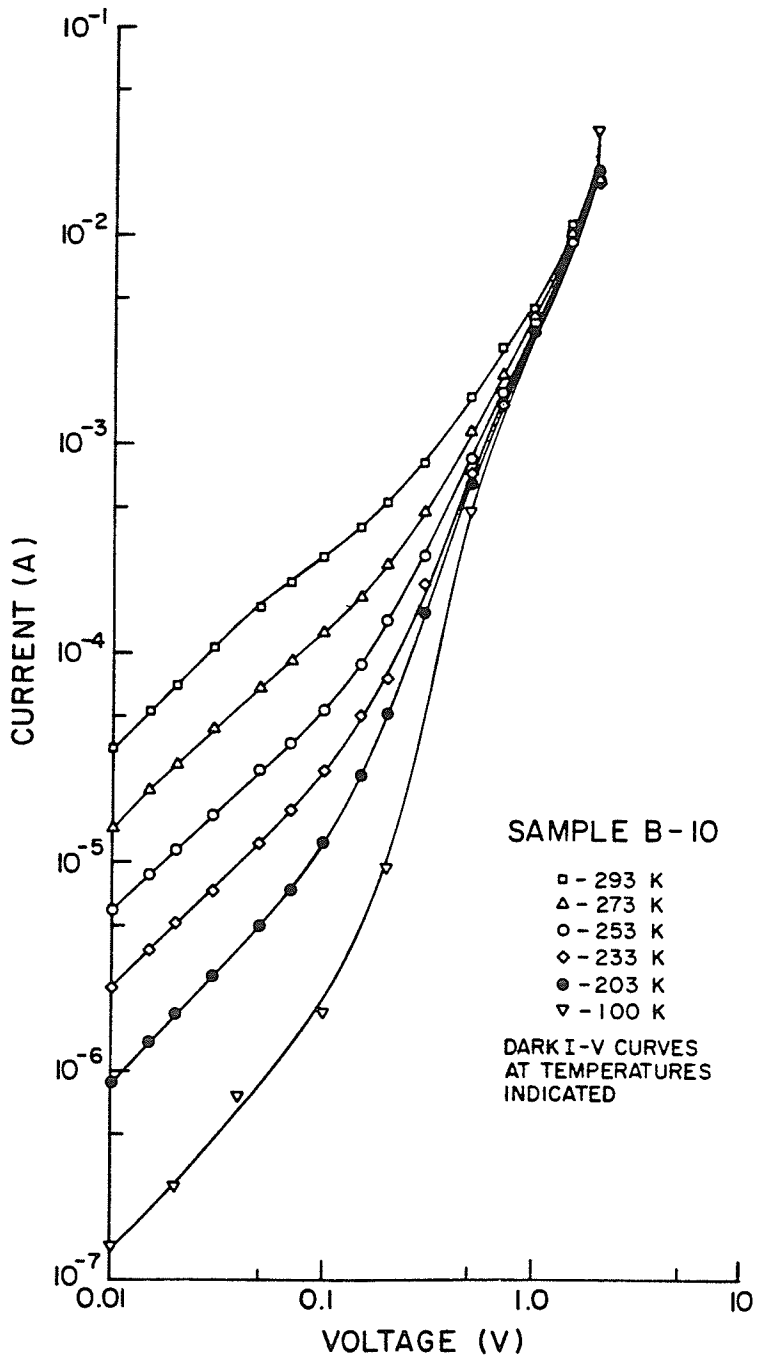

Fig. 3.4 Typical I-V characteristics of a nonuniform grain boundary (sample B-10) at several measurement temperatures.

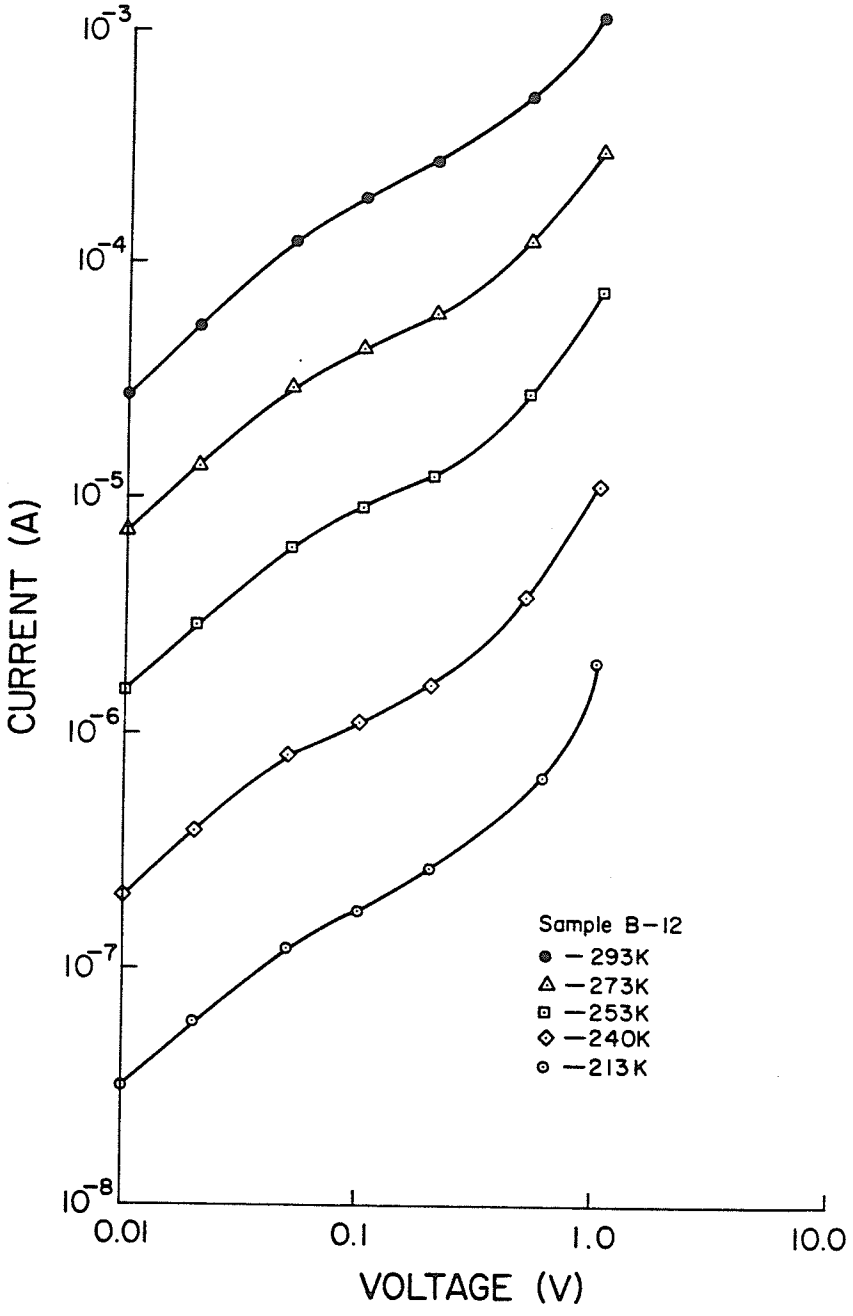

Fig. 3.5 Typical I-V characteristics of a uniform grain boundary (sample B- 12) at several measurement temperatures.

of E_a vs $1/T$ for three different grain boundaries is shown in Fig. 3.6. From this graph values for $< V_d >$ and σ were estimated and found to be $< V_d > \simeq 0.59V$ and $\sigma \simeq 0.10V$ for sample B-10, $< V_d > \simeq 0.70V$ and $\sigma \simeq 0.11V$ for sample B-9, and $< V_d > \simeq 0.32V$ and $\sigma \simeq 0.00V$ for sample B-12. The two similar values (B-9 and B-10) were obtained on separate samples cut from the same grain boundary in the Wacker silicon, and show a consistency in the observed fluctuations and magnitude of grain-boundary diffusion potential. The grain boundary in sample B-12 alone appears to be spatially uniform in its properties, as $\sigma \simeq 0$, indicating no variation of diffusion potential over this boundary. It should also be noted that in the case of the uniform boundary B-12 the current density calculated from eqn. 3.4 (using $V_{do} = 0.32$) agrees closely with the measured current density.

The accuracy of the fit to the gaussian model for samples B-9 and B-10 is approxiately 20% for $< V_d >$ and 10% for σ. This accuracy could naturally be improved by assuming more realistic statistical ditributions for the diffusion potential, or by including more terms in a series expansion of an arbitrary distribution function.

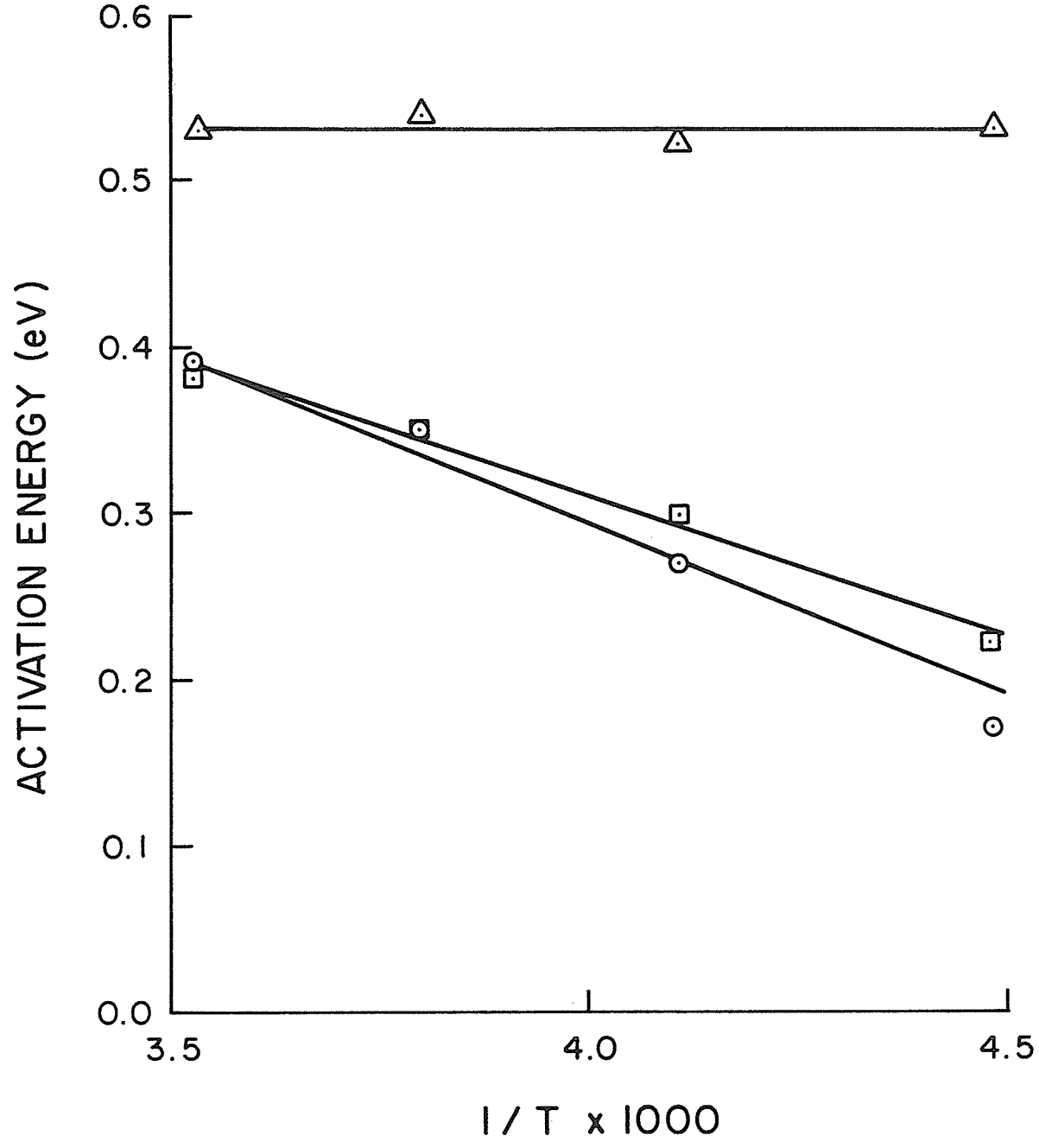

Fig. 3.6 A plot of $E_a(T)$ vs 1/T for several grain boundaries.

3.3 Conclusions

It is improper to generally assume that grain boundaries in cast semicrystalline silicon are spatially uniform in interface potential. Observed non-uniformities can be modelled to a first approximation by a gaussian distribution of diffusion potentials, which may be interpreted as originating from spatial variations in either interface state density or impurity segration to the grain boundary as reported in [35]. In Wacker silicon 'Silso' material boundaries have been found with average diffusion potentials $< V_d >$ as large as 0.70V and standard deviations σ up to 0.11V.

CHAPTER IV

Fabrication and Characterization of Grating-Structure Solar Cells*

4.1 Introduction

In the search for economical solar energy conversion using silicon photovoltaic cells, several device structures have been proposed or investigated which are alternatives to the conventional p-n junction solar cell. One category of these alternative devices may be generally classified as 'grating' solar cells. While the conventional diffused p-n junction device itself requires a grating structure as an electrode to the heavily-doped surface region, this grating is on a considerably coarser scale than those employed in the cells described here. We will therefore adopt the convention that grating solar cells are those in which the top metallization is in the form of a fine grid, and in which no diffused (or ion-implanted) p-n junction exists over the active (photosensitive) area of the device. This convention also excludes the normal case of the Schottky barrier solar cell[37,38] in which a metal-silicon junction exists over the entire active area.

We may further subdivide grating solar cells into two groups, depending upon whether the dark currents in these devices are predominantly due to majority or minority carriers in the silicon, and refer to these as majority and minority carrier grating solar cells. This is a similar terminology to that of Shewchun et al for MIS devices[39].

---

*The contents of this chapter have been submitted for publication to Solar Cells; October 1982.

Grating solar cells have been studied by several authors. The minority-carrier grating solar cells have received the overwhelming majority of this attention, with excellent theoretical and experimental results[40-42]. These devices are often also referred to as minMIS solar cells[40]. On the other hand, majority-carrier grating solar cells have previously been proposed and investigated theoretically,[43,44] but no experimental studies have been reported for these interesting devices. One study which we reported earlier[45] has contributed indirect experimental information concerning these cells, but no complete solar cell structure was presented in that work.

In this chapter we describe the fabrication and the photovoltaic characteristics of majority-carrier grating solar cells. In the development of these devices we have also incorporated substantial improvements from the use of 'peaked' Schottky barriers[46] at the grating-silicon interface. In addition we provide, for comparison purposes, similar data for minority-carrier or minMIS grating solar cells fabricated under identical conditions in our laboratory. Comparisons between crystalline and cast polycrystalline silicon substrate materials are also made. A classification of our grating cells is shown in Fig. 4.1.

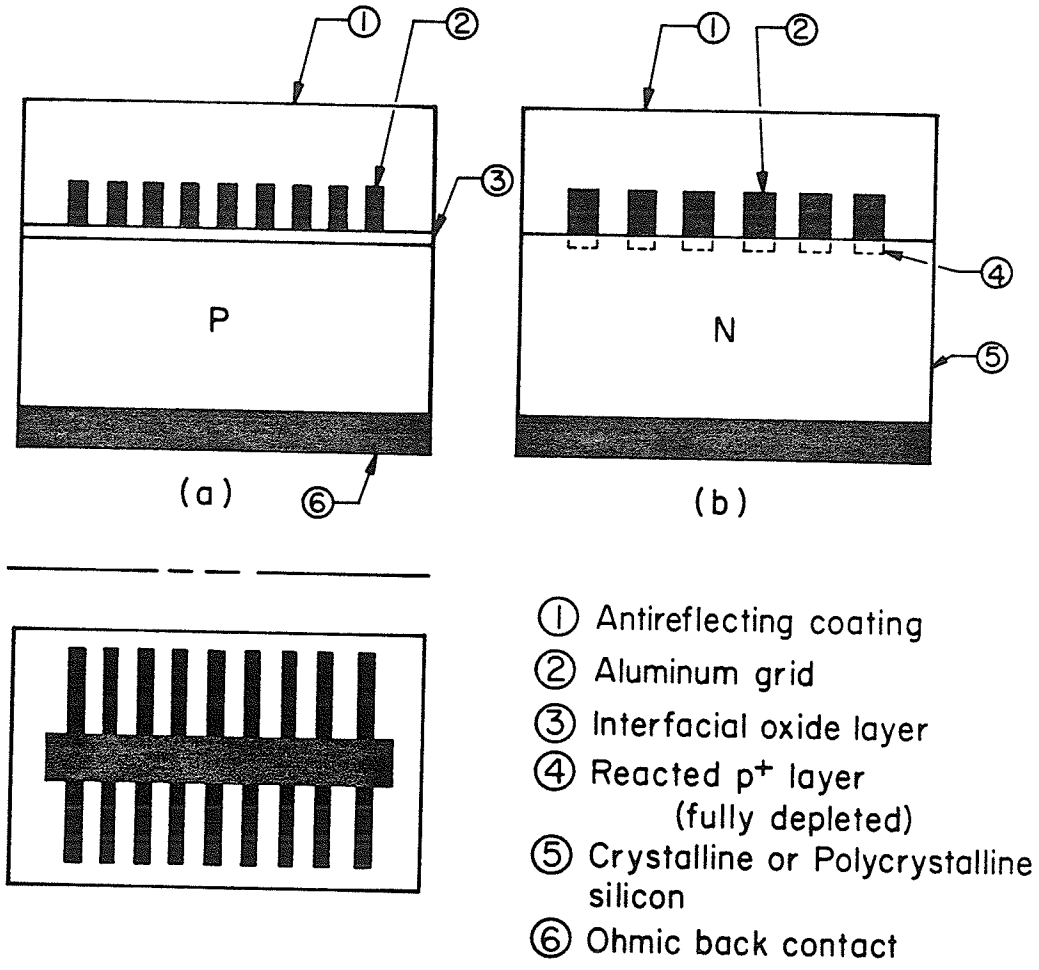

Grating Solar Cells

(a) Minority Carrier (min MIS) Cell.

(b) Majority Carrier (Peaked Schottky Barrier) Cell.

Fig. 4.1 The structure of the minMIS (a) and majority-carrier (b) grating solar cell.

4.2 Experimental Details

The silicon materials used in these studies were p and n type (111) oriented crystalline wafers obtained from Semimetals Inc. with doping concentrations of $N_a = 1.2 \times 10^{16}$ cm^{-3} and $N_d = 5 \times 10^{14}$ cm^{-3} respectively, and p-type cast polycrystalline wafers obtained from Wacker Chemitronic, Inc with $N_a = 3 \times 10^{15}$ cm^{-3}. The polycrystalline (Wacker Silso) material consisted of primarily columnar grains of typically 1 mm diameter in the plane of the surface, as discussed by Huber et al[47].

Fabrication techniques for the minority-carrier (minMIS) grating cells on p-type crystalline and polycrystalline silicon were very similar to those reported by Godfrey and Green.[40] Aluminum gratings were defined photolithographically be means of the fine-line mask shown in Fig. 4.2. The details of this process are given in the appendix. The metal fingers were of 25 μm width on 90 μm spacings with a thickness of ~ 0.6 μm. the active area of this mask is approximately 0.8 cm^2. In this case the active area refers to the area of the cell where direct collection of the sunlight can occur. While this mask design was not optimal for total area efficiency, it was a constant for all cells described in this work and avoids some problems associated with reduced metal coverage. Antireflection coatings were made using evaporated SiO of 90 nm thickness. The SiO was evaporated from a tantalum crucible. The evaporation of the SiO layers required approximately 5 mins to complete. The evaporation was judged to be complete when the surface of the silicon exhibited a medium-blue color. SiO layers of this hue were measured using a Varian interferometer and were found to be 90 nm ± 10 nm in thickness. The charge density in

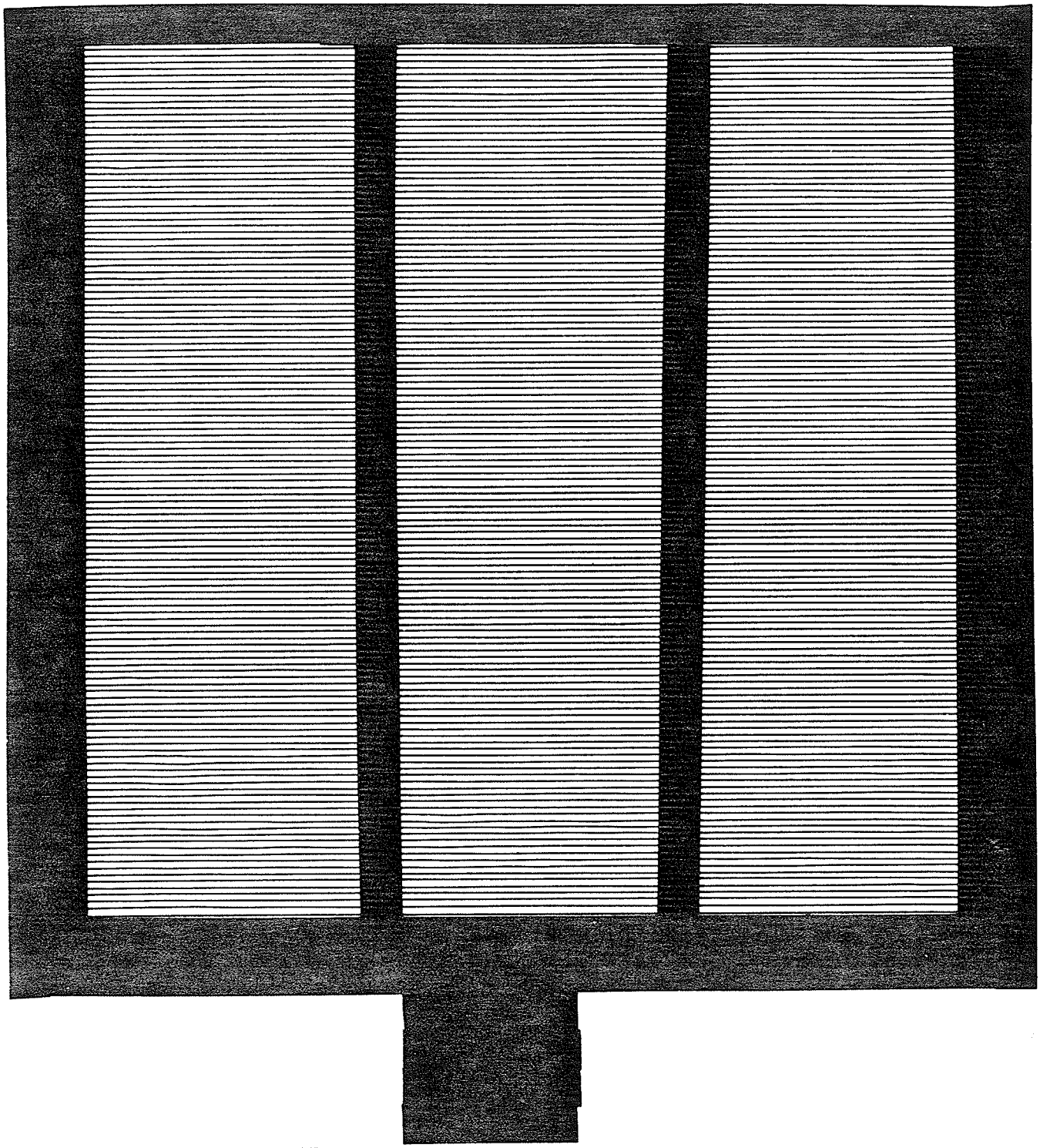

Fig. 4.2 The mask used in the fabrication of the grating structure solar cells.

these layers was also measured by standard MOS capacitor techniques[52] and was found to be 10^{13} cm^{-2}. This charge was measured over a period of days and was not found to change appreciably. The ohmic contacts for the minority-carrier cells were formed by sintering aluminum contacts at 600°C in a nitrogen ambient for 20 min. Residual H_2O vapor in the N_2 atmosphere leads to the formation of the required interfacial oxide layer on the upper surface, as reported elsewhere.[40]

Testing of the photovoltaic characteristics was done using both simulated and actual sunlight. In the case of laboratory simulation of sunlight, a GE ELH quartz-halogen lamp was employed to duplicate the short-circuit current obtained under natural sunlight (AM1) conditions. Spectral response measurements were made using a set of bandpass interference filters, with bandwidths of 50-70 nm, and the GE ELH source.

In the case of the majority carrier grating cells the fabrication process was considerably simpler. First a grating of aluminum was defined photolithographically on an N on N^+ substrate where the N region is ~ 100 μm thick with $N_d = 5 \times 10^{14}$ cm^{-3}. Then without stripping the photoresist the sample was heat treated in flowing O_2 for 15-20 mins. and then cooled to room temperature in 2-5 mins. Temperatures in the range of 550-675°C were used in the heat treatment of various samples. This process serves both to remove the photoresist and to form the junction. The back surface was then roughened with 400

grit-emery paper and an aluminum contact was subsequently deposited. Finally an AR coating of 90 nm of SiO was deposited over the grid by vacuum evaporation from a tantalum boat. Electrical contact to the grid was then achieved by means of a thin copper strip which was silver-pasted to the aluminum pad, after abrasion of the pad with 400 grit-emery paper.

4.3 Results and Discussion

Examples of the photovoltaic characteristics of majority-carrier grating solar cells are shown in Fig. 4.3, for a range of heat-treatment temperatures. These devices correspond to Aℓ gratings on n-type crystalline silicon. As discussed above the fabrication sequence for these cells is relatively simple and the characteristics are reproducible. Some degradation effects are observed with prolonged exposure to (AM1) illumination. This is associated with electrostatic charging of the antireflection coating and can be eliminated by "zerostat" anti-static techniques as described by Lam et al[48] for minority-carrier grating cells.

It should be noted that for the majority carrier devices, the positive charge in the antireflection (AR) coating acts to reflect minority carriers away from the surface rather than to attract them as in minMIS devices. The majority-carrier cells have proven consistently to be more stable than the minMIS cells in our studies. We attribute this to the relative insensitivity of the majority cells to the charge in the AR coating, which, unlike in the minority cells, affects the efficiency only through its effect on the surface recombination velocity.[44]

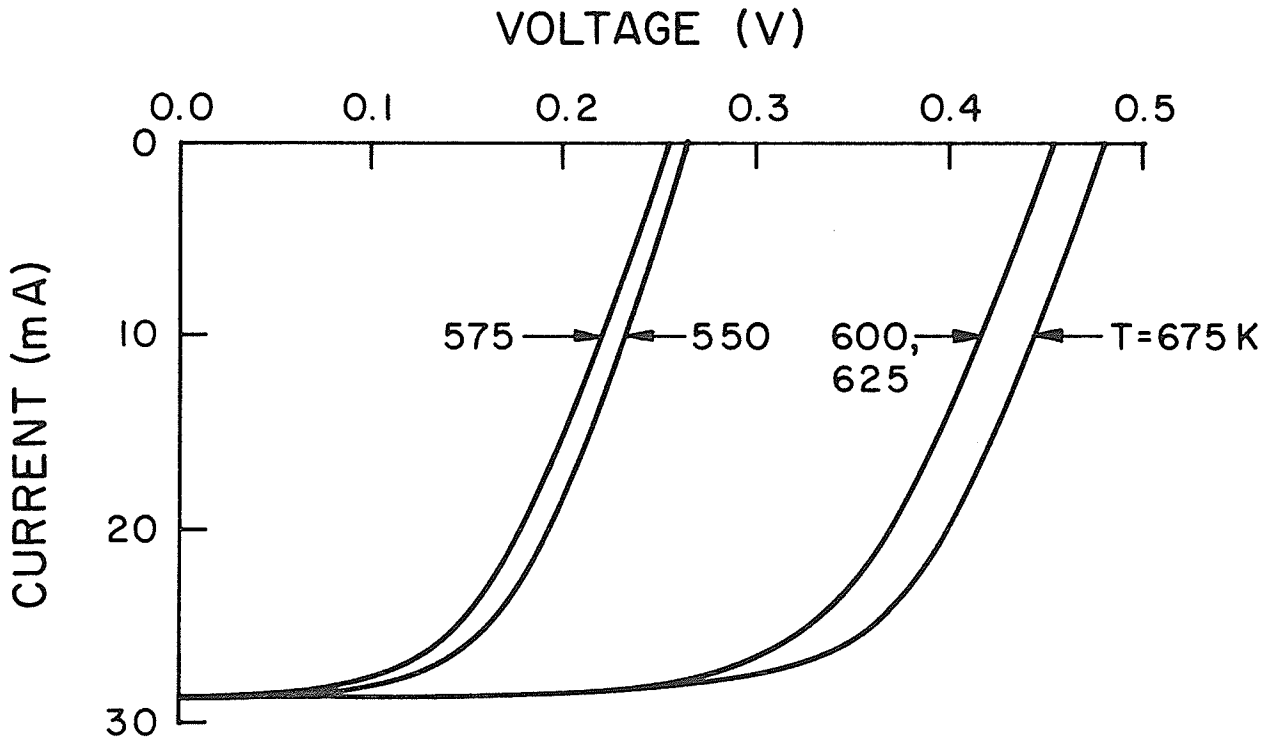

Fig. 4.3 The current vs voltage characteristics of majority-carrier solar cells under AM1 illumination for several heat treatment temperatures.

The grating-silicon interfaces were subjected to various degrees of heat treatment in order to promote metallurgical reactions as described earlier.[46,49] This results in so-called 'peaked' Schottky barriers with reduced dark currents. As predicted theoretically[46] the open-circuit voltage is enhanced by this procedure, and with it the photovoltaic efficiency. Figure 4.4 shows the increase in open-circuit voltage and photovoltaic efficiency with heat treatment. Above the Aℓ-Si eutectic temperature of 577°C, it is possible for a liquid phase to form during the heat treatment, resulting in an alloyed p-n junction. Below this temperature the height of the Schottky barrier is simply increased due to the existence of a fully-depleted p^+ region created by a solid-phase epitaxial regrowth of Si following heat treatment.[49] The formation of an alloyed p-n junction does not appear to form until well above the eutectic temperature, perhaps being inhibited by the interfacial oxide layer between the aluminum and silicon.[50] This is evidenced by the observation that, except for the most extreme heat treatment temperatures in Fig. 4.4, the open-circuit voltage remains below the value expected for a p-n junction in this material.

In Fig. 4.5 we show the photovoltaic characteristics of minority carrier (minMIS) grating cells which have been fabricated in our laboratory under similar conditions, with the same grating geometry and AR coatings. In Fig. 4.5, curve a corresponds to single-crystal silicon and curve b to cast polycrystalline silicon. Active area efficiencies are 14.0% and 10.3% for cases a and b respectively. The value

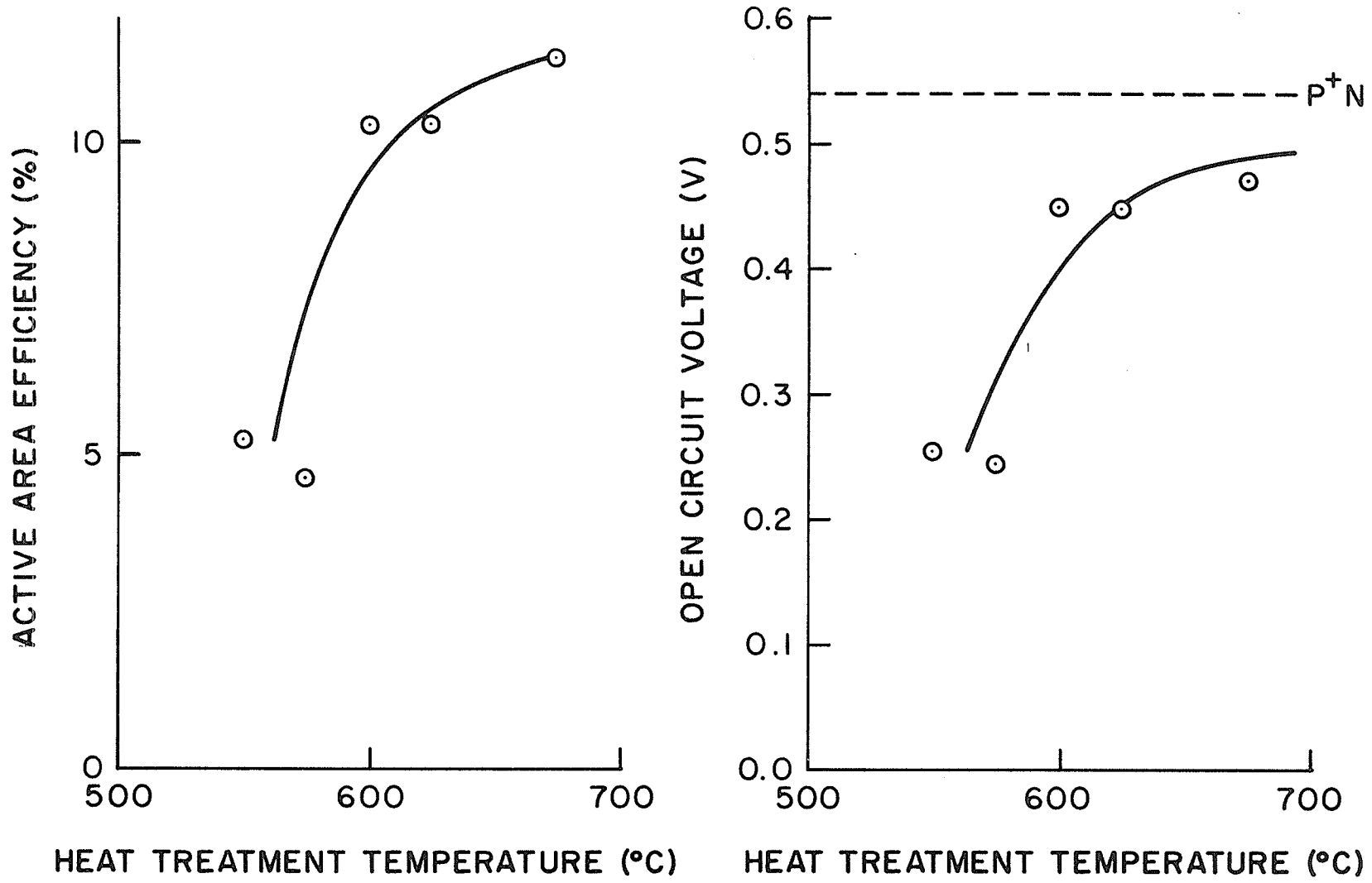

Fig. 4.4 The active area efficiency and the open circuit voltage of majority-carrier solar cells under AM1 illumination for several heat treatment temperatures.

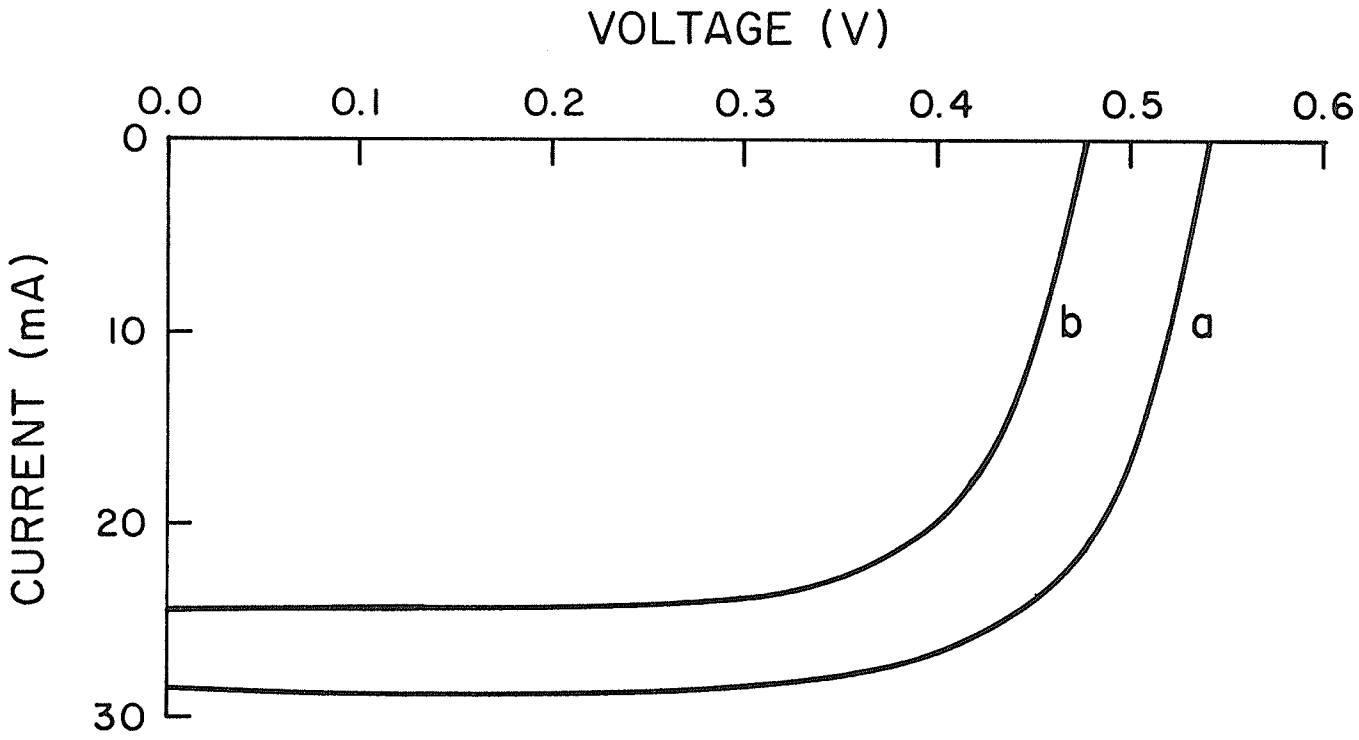

Fig. 4.5 The current vs voltage characteristics of minMIS solar cells under AM1 illumination for a crystalline (a) and polycrystalline (b) substrate.

for crystalline minMIS cells of 14.0% is to be compared with the best value of 11.4% observed for the peaked Schottky barrier majority-carrier grating cells above. This is due in part to the larger substrate doping in the p-type material used for the minMIS cells which increases the open-circuit voltage.[51] The short-circuit current in the majority-carrier cells is slightly larger than in the minMIS cells. The magnitude of these currents was established using natural sunlight, under AM1 conditions.

The spectral response of the grating solar cells was also measured, and was compared with that of a commercial diffused p-n junction cell. The response normalized to this commercial cell, i.e. $I_{grating}/I_{pn}$ is shown in Fig. 4.6(a) to (c) for the three cases discussed. In all cases, the response at short-wavelengths is better for the grating cells by as much as a factor of two. The long-wavelength response of the polycrystalline cell is inferior, as expected on the basis of the reduced diffusion length in this material-

.

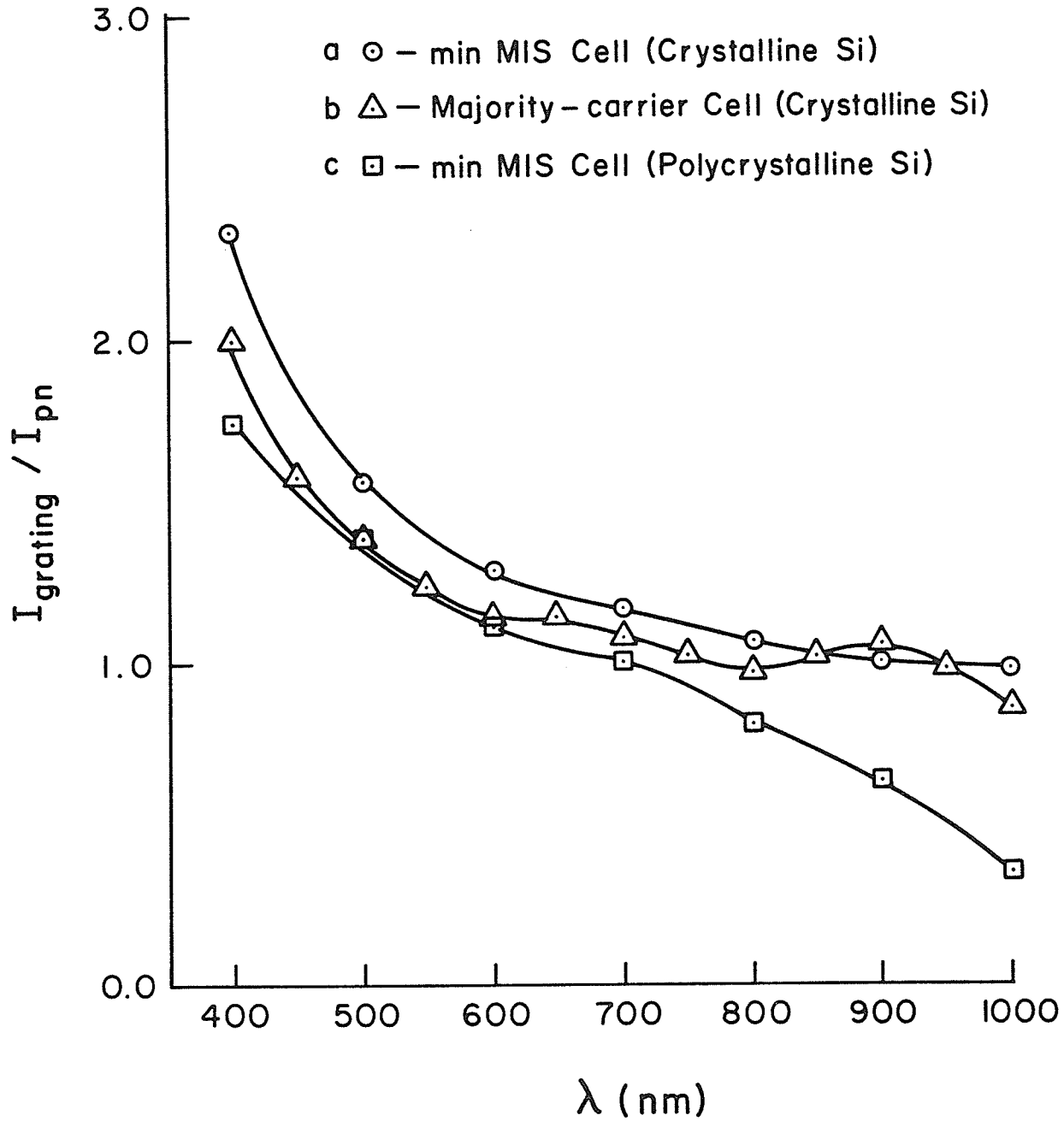

Fig. 4.6 The spectral response (short-circuit current density) of minMIS and majority-carrier solar cells with respect to a commercial p-n junction solar cell for wavelengths from 400-1000 nm.

4.4 Conclusions

Majority-carrier grating solar cells with respectable photovoltaic efficiencies can be prepared by a relatively simple fabrication technique. These devices are only slightly inferior to minority-carrier (minMIS) solar cells, and do not require the control of an ultrathin interfacial oxide layer between the grating metal and the silicon. Peaked Schottky barriers at the grating-silicon interface provide substantial enhancement of the photovoltaic performance of the majority-carrier cells. We also believe that the photovoltaic characteristics of the majority-carrier cells are inherently more stable than minMIS cells, due to the reduced dependence of their operation upon the magnitude of charge in the antireflection coatings.

CHAPTER V

High-Injection Condition at Extended Defects in Silicon: a Mechanism for Dependence of Lifetime on Photogeneration Rate.*

5.1 Introduction

There have recently been a number of experimental reports of an increase in the minority carrier diffusion length, L, or lifetime, τ, with optical illumination intensity in silicon solar cells.[53-60] It is generally observed that L increases substantially, even at low intensities (below AM1), for material such as EFG ribbon silicon,[55-57] whereas in crystalline (Czochralski or float-zone) silicon these effects are observed only under strongly concentrated sunlight intensities.[54,58-60] The explanations for these observations have involved isolated trapping centers, and have invoked the suggestions of trap saturation[53] and/or traps with multiple energy levels.[54-57]

In this chapter, we present new data concerning the dependence of quantum efficiency vs. wavelength upon the intensity of optical (white-light) bias, for silicon photovoltaic cells made from both cast (large-grained) polycrystalline silicon and crystalline silicon. We also show that the observed behaviour is consistent with minority carrier recombination at either grain boundaries or dislocations. As a

---

*This chapter was performed in collaboration with Mr. D.J. Mbewe; the contents have been submitted for publication to IEEE Transactions on Electron Devices; October 1982.

result of the space-charge regions adjacent to these extended defects,[8,31,61] conditions of high-level injection can occur in the polycrystalline material at relatively low optical intensities. It is the high-level injection condition, we argue, that causes the increase in carrier lifetime in accordance with Shockley-Read-Hall (SRH) statistics.[62,63] Neither trap saturation nor multilevel centers are required for this mechanism, although these complications may certainly be present in some cases. In crystalline material, recombination occurs primarily through isolated point defect centers, and in this case high-level injection is reached only under extremely high optical intensities for typical base doping levels of silicon solar cells.[14] Such intensities are only obtained in strongly concentrated sunlight (typically 100-1000 suns).

5.2 Experimental

The cast polycrystalline silicon used in the present studies was p-type 'Silso' material with an acceptor concentration $N_a = 3 \times 10^{15}$ cm^{-3} obtained from Wacker Chemitronic, Inc. Solar cell structures were of the 'minMIS' minority-carrier grating type, described in the previous chapter. Details on the fabrication, performance, and geometry of our devices are as described in Chapter IV.

The measurements of quantum efficiency vs. wavelength were performed using the arrangement shown in Fig. 5.1. A monochromatic optical excitation of 50-200 μW cm^{-2} was chopped at a frequency of 10 Hz, and the response (short-circuit current) was measured using phase-sensitive detection. At the same time, the sample was illuminated with an optical bias of (unchopped) white light from a General Electric ELH

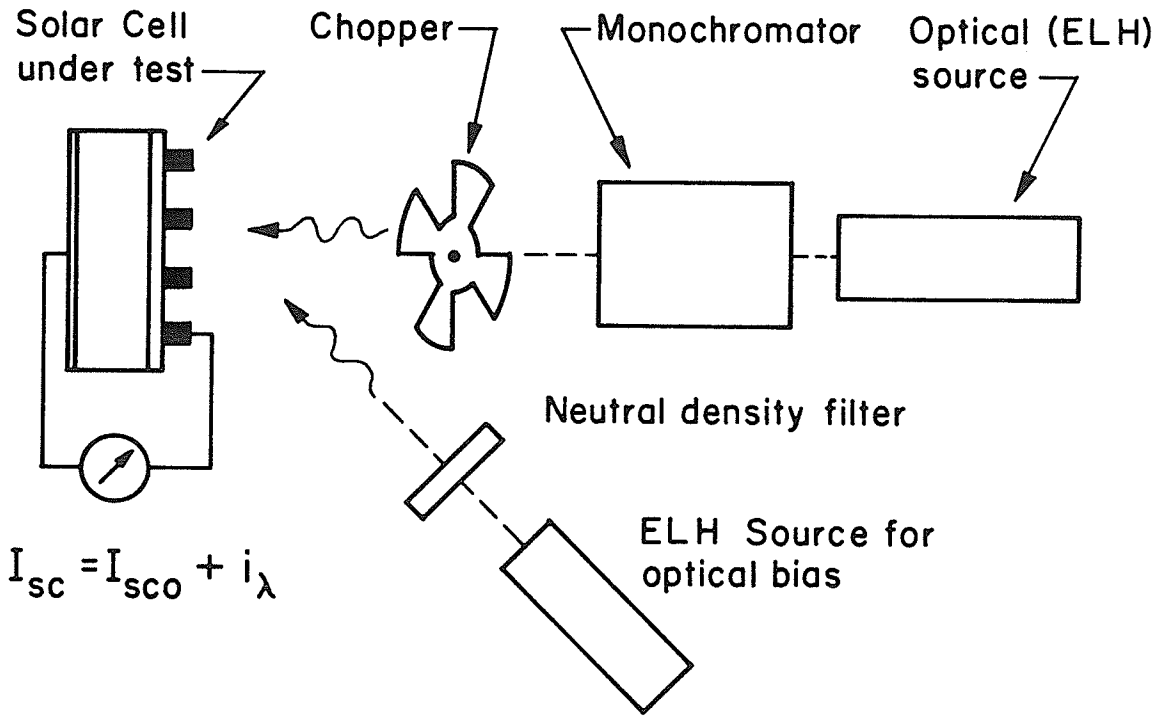

Fig. 5.1 Schematic experimental arrangement employed in obtaining results of Fig. 1 (no optical bias $I_{sc} = i_\lambda$) and Fig. 3 (with optical bias $I_{sc} = I_{sco} + i_\lambda$).

quartz-halogen lamp, the intensity of which was controlled using neutral density filters. Figure 5.2 shows a typical example of the spectral response of the polycrystalline silicon device in the absence of an optical white-light bias. Figure 5.3 shows the response of the same device with the intensity of the optical bias as a parameter. These results (Fig. 5.3) have been normalized to the response with no optical bias. It is apparent (a) that the response at longer wavelengths increases monotonically with the intensity of the optical bias, up to a factor of approximately two. The experiment has also been performed with crystalline silicon solar cells, and up to the maximum intensity (AM1) studied here no significant enhancement of the response due to the optical bias has been observed (the response is increased by at most 1-2% by the optical bias).

5.3 Discussion

Our interpretation of these results as well as those concerning the dependence of minority carrier diffusion length or lifetime observed earlier[55-57] relies upon the presence of extended defects: dislocations or grain boundaries in the Wacker (and ribbon) silicon materials. It is well known that in the cast silicon material such as the Wacker Silso type used here, recombination occurs both at the grain boundaries and at dislocations within the grains themselves. Since the grain size is large, the majority of the recombination is likely to occur at dislocations. The density of these dislocations is much greater than in Czochralski or float-zone crystalline silicon material, as a result of the casting process.

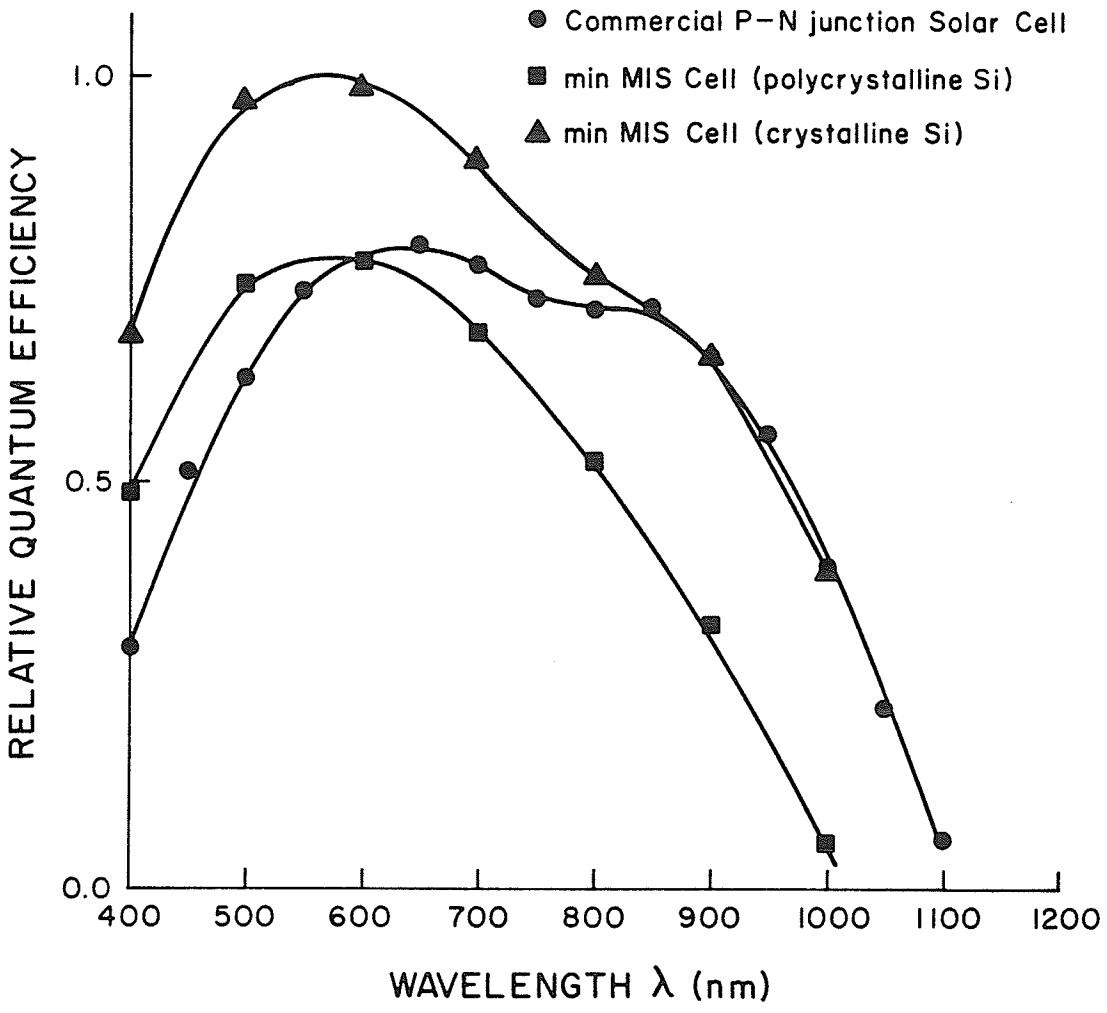

Fig. 5.2 Spectral response (quantum efficiency) of minMIS solar cells made from p-type Wacker'Silso' cast polycrystalline silicon, and from crystalline Czochralski silicon. Obtained from short-circuit current measurements.

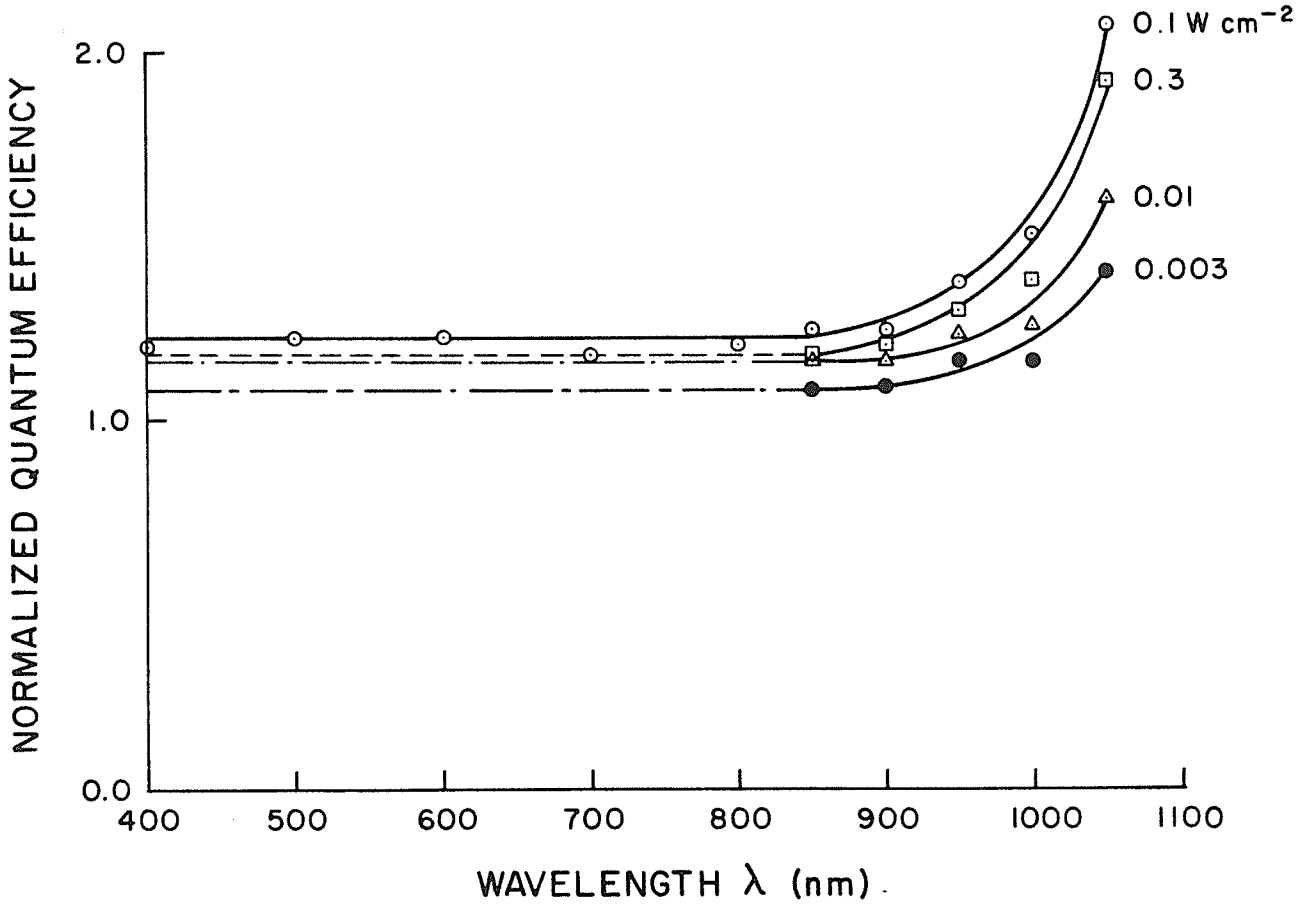

Fig. 5.3 Spectral response of minMIS solar cells made from p-type Wacker 'Silso' cast polycrystalline silicon, with the intensity of an optical bias (white light from GE ELH lamp) as a parameter (normalized to result in absence of optical bias, Fig. 2). Obtained from incremental response of short-circuit current to chopped monochromatic light of low intensity.

Figure 5.4 shows the energy-band diagram in the neighborhood of a dislocation or grain boundary, as discussed previously.[8] The position (x) from the defect is measured radially in the case of a dislocation (line defect) or perpendicular from the grain boundary (planar defect).

We assume that their exists a single level of localized states or traps at the defect, which is somewhat broadened by the variation in the atomic configurations surrounding this defect. This level is approximately at midgap, with a spread of less than 0.1 eV, as determined experimentally for silicon bicrystals or grain boundaries.[31] The origin of the primary defect is probably an unsatisfied or 'dangling' bond on a silicon atom. The density of these defects is on the order of 10^{11}-10^{12} cm^{-2}.[12,65] For any appreciable illumination intensity, the quasi-Fermi levels for electrons and holes enclose these defect centers in energy, so that all of the states in this peak contribute equally to recombination.[8,26] According to SRH statistics the recombination rate of electrons and holes through these centers is given by[8,62]

$$R = \frac{N_t V_{th} \sigma_n \sigma_p (pn - n_i^2)}{\sigma_n(n+n_1) + \sigma_p(p+p_1)} \qquad (5.1)$$

where n and p are the concentrations of electrons and holes at the defect site, N_t is the density of traps, V_{th} is the thermal velocity, σ_n and σ_p are the capture cross sections of the traps for electrons and holes, n_i is the intrinsic carrier concentration, and

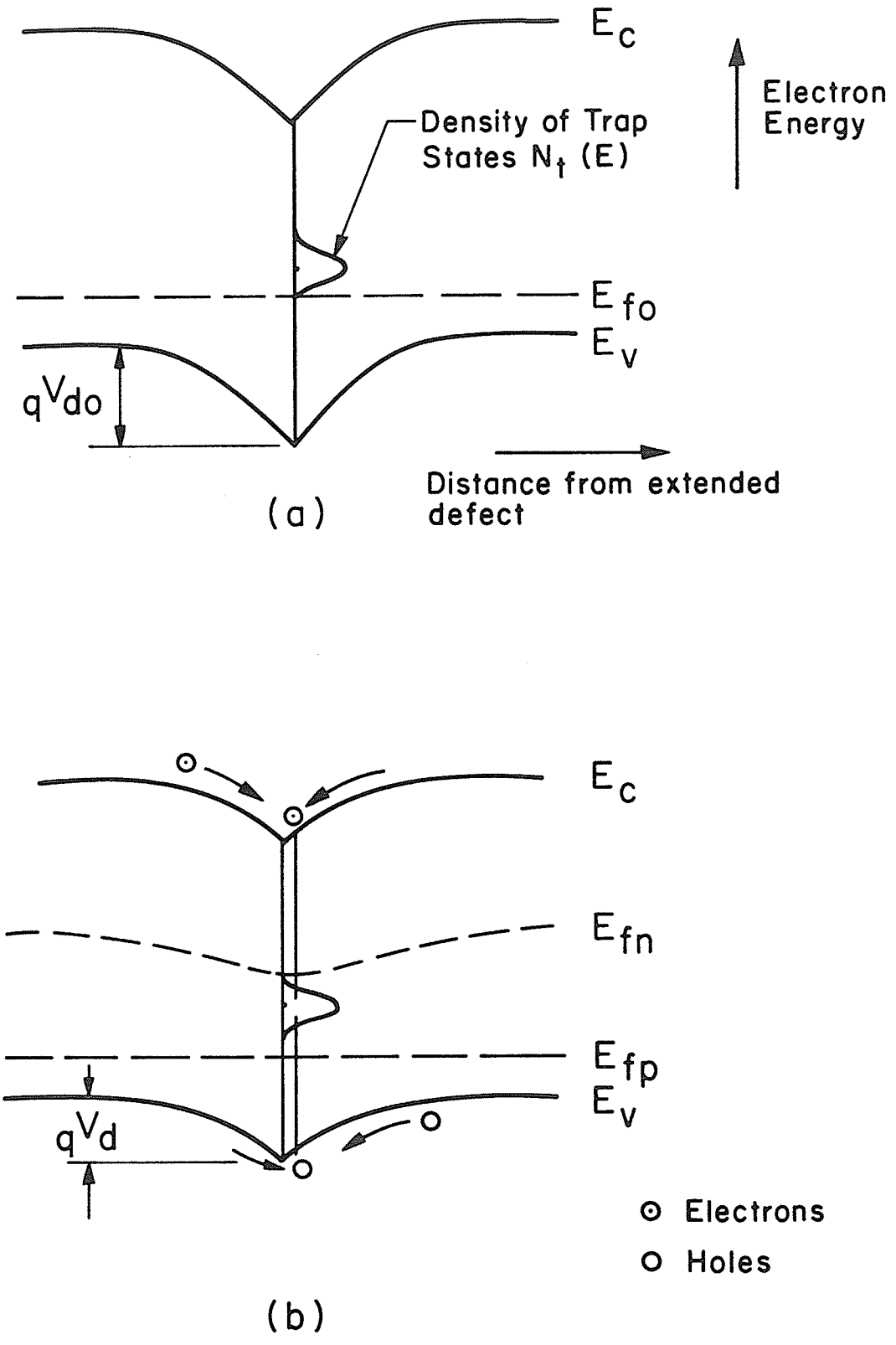

Fig. 5.4 Energy-band diagram in neighborhood of extended defect in Silicon (a) in equilibrium, and (b) under appreciable optical illumination. Superimposed on these figures is a schematic distribution of trap states, or recombination centers.

$$n_1 = n_i \exp\left(\frac{E_t - E_i}{kT}\right) \tag{5.2}$$

$$p_1 = n_i \exp\left(\frac{E_i - E_t}{kT}\right) \tag{5.3}$$

with E_i the intrinsic (midgap) energy level and E_t the energy level of the traps. To a first approximation, since we assume as discussed above that $E_t \approx E_i$, n_1 and p_1 are of the order of n_i, the intrinsic concentration.

To be specific, let us consider p-type silicon material, as in Fig. 5.4 and as in the samples of Figs. 5.2 and 5.3. As is known from work on silicon grain boundries, the trapping states in p-type material take on a positive charge which is compensated by a negative charge in the surrounding silicon so that a space-charge (depletion) region of uncompensated acceptors develops adjacent to the defect.[65] Parenthetically, it is significant that in n-type material the traps assume a negative charge and again a depletion region is established, this time of uncompensated donors.[12] These observations imply a neutral level for the traps near midgap, which suggests an admixture of donor-like and acceptor-like character for these traps.

The density of traps N_t will determine the energy position of the equilibrium Fermi level E_{fo} at the defect site, with E_{fo} approaching midgap at large N_t. Assuming an intermediate value of N_t for generality we have that $n \ll p$ at the defect under equili-

brium (dark) conditions. Eqn. (1) therefore simplifies, near equilibrium, to

$$R \simeq N_t V_{th} \sigma_n (n - n_o) \tag{5.4}$$

where n_1 , p_1 have been neglected in comparison with p and n_o is the equilibrium concentration of electrons at the defect.

R in Eqns. (5.1) and (5.4) has units of $m^{-2}s^{-1}$ for planar defects (grain boundaries) and $m^{-1}s^{-1}$ for linear defects (dislocations). N_t has units m^{-2} and m-1 in the two cases. The units of V_{th} , σ_n and n are ms^{-1}, m^2 and m^{-3} in both cases.

In order to obtain the <u>volume</u> recombination rates, we recognize that the density of traps per unit volume is given by

$$N_{tv} = \frac{1}{V} \int_A N_t \cdot dA \qquad \text{planar defects} \tag{5.5a}$$

$$= \frac{1}{V} \int_\ell N_t \cdot d\ell \qquad \text{linear defects} \tag{5.5b}$$

where the integrals are over the total area or length of the defects in the sample volume. Similarly we can write for the volume recombination rates,

$$R_v = \frac{1}{V} \int_A R \cdot dA \qquad \text{planar defects} \tag{5.6a}$$

$$= \frac{1}{V} \int_{\ell} R \cdot d\ell \qquad \text{linear defects} \qquad (5.6b)$$

We can alternatively write an expression for the volume recombination rates which involves the minority carrier lifetime τ_n as

$$R_v = \frac{n_v - n_{vo}}{\tau_n} \qquad (5.7)$$

provided $n_v \ll p_v$, where n_v and p_v are the volume concentrations of electrons and holes under conditions of optical illumination and n_{vo}, p_{vo} are the equilibrium values of n_i^2/N_a and N_a respectively. N_a is the acceptor doping concentration of the material.

The concentration n_v of electrons in the bulk material, away from the defects, is substantially lower than n at the defect site, as a consequence of the reduced potential energy for electrons there (Fig. 5.4). The relation for the equilibrium (dark) case is simply

$$n_o = n_{vo} \exp(V_{do}/V_T) \qquad (5.8)$$

where V_{do} is the equilibrium diffusion potential in Fig. 5.4 and $V_T = kT/q$. Under conditions of optical illumination, however, the relationship of n to n_v is complicated by the uncertainty in the shape of the electron quasi-Fermi level E_{fn} which is no longer flat through the space-charge region[26] particularly at high recombination rates.

If we employ the reasonable assumption that E_{fn} remains approximately flat under conditions of low illumination, and the diffusion potential is not modified from V_{do}, then n and n_v are also related by Eqn. (5.8).

$$n = n_v \exp(V_{do}/V_T) \tag{5.9}$$

for low illumination levels. Note that V_{do} remains in (5.9) because for low photogeneration rates the diffusion potential V_d maintains its equilibrium value V_{do}[8,65].

Assuming defects with uniform properties over the length or area of the dislocation or grain boundary, we obtain from Eqns. (5.5) and (5.6) that

$$R_v = R\left(\frac{N_{tv}}{N_t}\right) \tag{5.10}$$

which with Eqns. (5.4), (5.8), and (5.9) gives that

$$R_v = N_{tv} V_{th} \sigma_n (n_v - n_{vo}) \exp\left(\frac{V_{do}}{V_T}\right) \tag{5.11}$$

Using (7),

$$\tau_n = \left(N_{tv} V_{th} \sigma_n \exp(V_{do}/V_T)\right)^{-1} \tag{5.12}$$

for sufficiently low photogeneration rates that the diffusion potential V_d remains at its equilibrium value V_{do}. One can regard Eqn. (5.12) as the normal expression for lifetime under low-injection conditions, except that an effective capture cross section

$$\sigma_n^* = \sigma_n \exp\left(\frac{V_{do}}{V_T}\right) \tag{5.13}$$

is associated with the recombination centers for the extended defects.

As the photogeneration rate increases, the concentration of minority carriers at the defect n increases as this is an imperfect sink for these carriers, until at a critical illumination intensity $n \sigma_n \simeq p \sigma_p$ at the defect. At this point, V_d will begin to decrease rapidly from its equilibrium value V_{do} with further increases in illumination intensity.[8,26] This marks the onset of high injection conditions at the defect, with n and p increasing with illumination in such a way that $n \sigma_n \simeq p \sigma_p$ thereafter.[8] Under these conditions, (5.1) may be rewritten as

$$R \simeq \frac{N_t V_{th} \sigma_n n}{2} = \frac{N_t V_{th} \sigma_p p}{2} \tag{5.14}$$

and

$$R_v \simeq \frac{N_{tv} V_{th} \sigma_n \exp\left(\frac{V_d}{V_T}\right) n_v}{2} \tag{5.15}$$

so that

$$\tau_n = 2\left(N_{tv}\, V_{th}\, \sigma_n \exp\left(\frac{V_d}{V_T}\right)\right)^{-1} \qquad (5.16)$$

for high-level injection conditions at the defect. Thus the effective capture cross section becomes

$$\sigma_n^* = \frac{1}{2}\,\sigma_n \exp\left(\frac{V_d}{V_T}\right) \qquad (5.17)$$

for high photogeneration rates. Eqn. (5.16) shows that the lifetime for high optical illumination intensities is larger than that at low intensities by at least a factor of two, and can be considerably larger for appreciable decreases in V_d below V_{do}.

The experimental results of Fig. 5.3 imply that the minority carrier diffusion length L_n of the solar cell increases by a factor of approximately two as the optical intensity increases to the AM1 level, for the Wacker silicon in which the recombination is controlled by extended defects such as dislocations or grain boundaries. An observed increase in L_n by a factor of two translates into an increase in minority carrier lifetime τ_n by a factor of four, since $L_n = (D_n\, \tau_n)^{1/2}$, which is a very reasonable value in the light of Eqn. (5.16). This corresponds to the observed spectral response at long wavelengths (near-uniform photogeneration) which increases by this same factor of two.

It is important to note that the optical intensity required for the onset of the increased lifetime may be relatively low provided the diffusion potential V_{do} at the extended defects is large. In the limit of $V_{do} \simeq E_g/2q$ with E_g the energy gap, the high-injection condition at the defect $(n\,\sigma_n \simeq p\,\sigma_p)$ occurs at virtually all illumination intensities. High-injection effects for bulk recombination through point defects (as expected in crystalline material) occurs only when $n_v \sigma_n \simeq p_v \sigma_p$, which is usually only under concentrated sunlight for extrinsic silicon.(66)

We believe that the above model explains the enhanced spectral response at long wavelengths under optical bias shown in Fig. 5.3, the absence of these effects in solar cells made from crystalline silicon, and the earlier observations of these effects in ribbon silicon cells. The photoresponse of the polycrystalline Si devices without optical bias, as shown in Fig. 5.2, is only 25% to 75% of that for the crystalline devices (depending upon λ) over the wavelength range of interest. With the optical bias, however, the response of the polycrystalline devices (but not the crystalline devices) is improved. This results in an AM1 short-circuit current density only marginally smaller in the polycrystalline than in the crystalline case. The present explanation does not depend upon assumptions of multilevel centers or trap saturation, but only upon the established presence of space-charge regions surrounding extended defects (dislocations and grain boundaries) in the cast (polycrystalline) and ribbon silicon materials.(67)

It has been determined that for minMIS solar cells on crystalline (Czochralski) silicon fabricated in our laboratory, the

short-circuit current density under AM1 conditions is 35 mA cm^{-2} . In identical cells made from Wacker Silso silicon, the short-circuit current density falls only slightly, to 30.5 mA cm^{-2}. This is shown in Fig. 5.5; compare the characteristics of (a) and (c). Device (b) is of a different type in which the photocurrent is the same as (a), but the dark current is comparable to (c). In cases (a) and (c) the silicon is p-type; in (b) it is n-type and the grating is reacted with the silicon to form a 'peaked' Schottky barrier. The minor reductions in short-circuit current from (a) to (c) are consistent with the beneficial effects of the AM1 optical bias upon the spectral response for the Wacker material alone, allowing it to perform nearly as well as the crystalline silicon which is not affected by the optical bias at this illumination level.

5.4 Conclusions

It is a property of recombination through extended defects (dislocations, grain boundaries) in extrinsic silicon that the recombination lifetime of minority carriers may be appreciably enhanced by relatively low levels of optical illumination (below AM1). This is not the case for extrinsic crystalline silicon in which recombination occurs through point defects. The origin of the difference is the space-charge regions which accompany extended defects, and which lead to the onset of high-injection conditions at the defect sites at low illumination levels. This also results in a simple modification of the expression for capture cross sections of these defects. The present model accounts for our experimental observations (1) that the quantum efficiency at long wavelengths, of solar cells on silicon containing

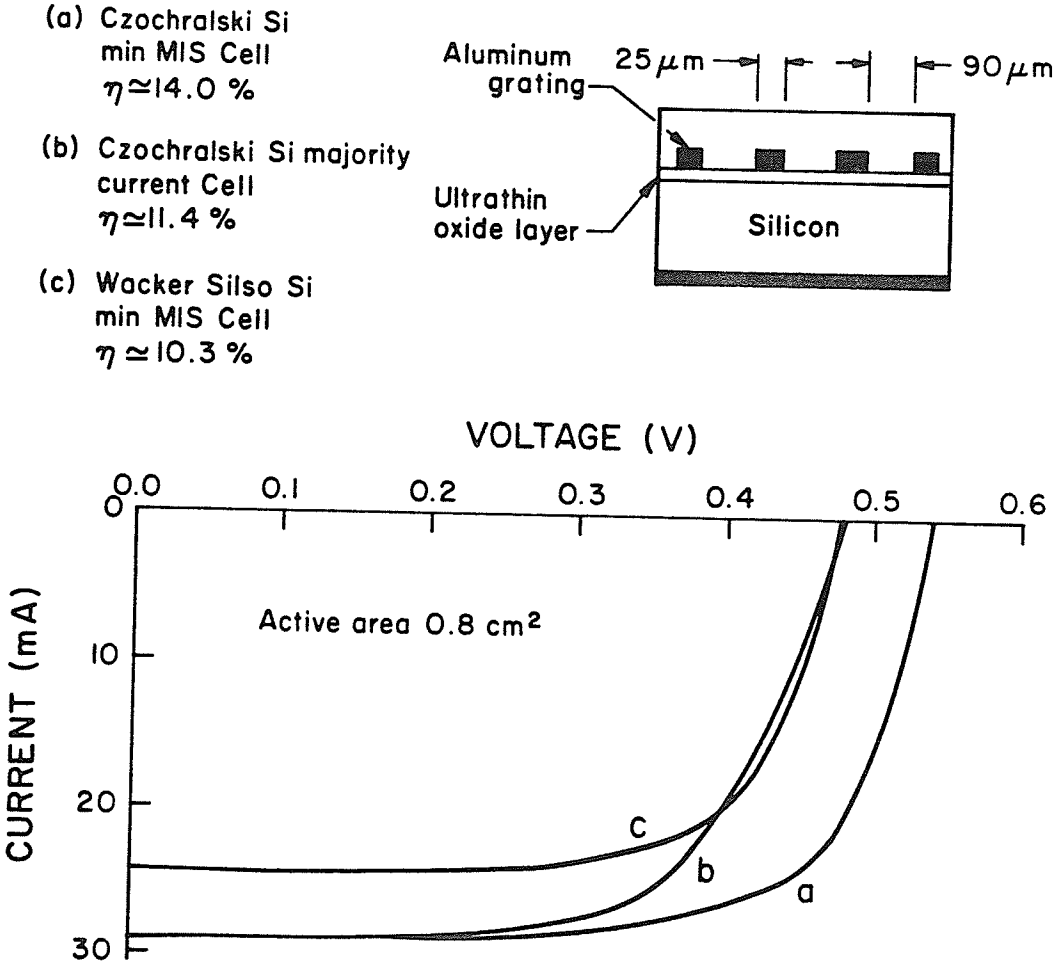

Fig. 5.5 Characteristics of grating solar cells; described in detail in Ref. (16). Note that a modest reduction in short-circuit current is experienced in changing from crystalline to Wacker silicon (curves (a) and (c) respectively).

extended defects, is substantially improved by an optical bias, (2) that the photocurrents in these devices are not appreciably reduced below those in Czochralski silicon cells, and (3) that the improvement of spectral response in the crystalline case can only occur at much higher optical intensities (concentrated sunlight), when high-level injection conditions are achieved in the bulk of the silicon.

CHAPTER VI

Conclusions

On the basis of the experimental studies described in Chapter II, and the theoretical arguments concerning the collection velocity of the grain boundary for majority carriers, the rate-limiting process of diffusion to the grain boundary should be incorporated into the majority carrier transport model. Grain boundaries with a variety of diffusion potentials exist[29] in Wacker 'Silso' silicon, and many of these boundaries contain potential barriers which are spatially-nonuniform over macroscopic portions of the grain-boundary plane. The spatially-nonuniform boundaries conform reasonably well to a Gaussian distribution of electrostatic potential over the sample area, with standard deviation σ as large as 0.11 eV . Spatially-uniform grain boundaries also exist in this material, and for these samples a reasonable agreement with the theoretical predictions of Shaw and Card[13] is obtained. Grain-boundary interface-state densities N_{is} measured in this material are in the range of 10^{15} to 10^{16} m^{-2} eV^{-1} and exhibit an increase with increasing energy in the lower half of the energy gap between $E_v + 0.3$ and $E_v + 0.5$ eV . It is suggested that direct measurements of these interface-state distributions by techniques such as depleted-layer spectroscopy[30] are necessary for accurate determinations of N_{is} , since the results are otherwise transport-model dependent.

Majority-carrier grating solar cells with respectable photovoltaic efficiencies can be prepared by a relatively simple fabrication technique. These devices are only slightly inferior to minority-carrier (minMIS) solar cells, and do not require the control of an ultrathin interfacial oxide layer between the grating metal and the silicon. Peaked Schottky barriers at the grating-silicon interface provide substantial enhancement of the photovoltaic performance of the majority-carrier cells. We also believe that the photovoltaic characteristics of the majority-carrier cells are inherently more stable than minMIS cells, due to the reduced dependence of their operation upon the magnitude charge in the antireflection coatings.

It is a property of recombination through extended defects (disloctions, grain boundaries) in extrinsic silicon that the recombination lifetime of minority carriers may be appreciably enhanced by relatively low levels of optical illumination (below AM1). A model based upon this property can accound for our experimental observations (1) that the quantum efficiency at long wavelengths, of solar cells on silicon containing extended defects, is substantially improved by an optical bias, (2) that the photocurrents in polysilicon devices are not appreciably reduced below those in Czochralski silicon cells, and (3) that the improvement of the spectral response in the crystalline case can only occur at much higher optical intensities (concentrated sunlight), when high-level injection conditions are achieved in the bulk of the silicon.

References

1. J. Volger, "Note on the Hall Potential Across an Inhomogeneous Conductor", Phys. Rev., Vol. 9, pp. 1023-1024, 1950.

2. R.L. Petritz, "Theory of Photoconductivity in Semiconductor Films", Phys. Rev., Vol. 104, pp. 1508-1518, 1956.

3. F.L. Vogel, W.T. Read, and L.C. Lovell, "Recombination of Holes and Electrons at Lineage Boundaries in Germanium', Phys. Rev., Vol. 94, pp. 1791-1972, 1954.

4. W.E. Taylor, N.H. Odell and H.Y. Fan, "Grain Boundary Barriers in Germanium", Phys. Rev., Vol. 88, pp. 867-875, 1952.

5. P.K. Mueller, "Current Flow across Grain Boundaries in n-Type Germanium - I", J. Appl. Phys., Vol. 32, pp. 635-639, 1961.

6. H.F. Matare, D.C. Cronemeyer, and M.W. Beaubien, "Germanium Bi-crystal Photoresponse - I", Solid-State Electronics, Vol. 7, pp. 583-588, 1964.

7. J.Y.W. Seto, "The Electrical Properties of Polycrystalline Silicon Films", J. Appl. Phys., Vol. 46, pp. 5247-5254, 1975.

8. H.C. Card and E.S. Yang, "Electronic Processes at Grain Boundaries in Polycrystalline Semiconductors Under Optical Illumination", IEEE Trans. Elec. Dev., Vol. ED-24, pp. 397-402, 1977.

9. L.L. Kazmerski, "The Effects of Grain Boundary and Interface Recombination on the Performance of Thin-film Solar Cells", Solid State Electronics, Vol. 21, pp. 1545-1550, 1978.

10. G.E. Pike and C.H. Seager, "The dc voltage dependence of semiconductor grain-boundary resistance", J. Appl. Phys., Vol. 50, pp. 3414-3422, 1979.

11. C.H. Seager, G.E. Pike, and D.S. Ginley, "Direct Measurement of Electron Emission from Defect States at Silicon Grain Boundaries", Phys. Rev. Lett., Vol. 43, pp. 532-535, 1975.

12. C.H. Seager and G.E. Pike, "Grain-boundary states and varistor behaviour in silicon bicrystals", Appl. Phys. Lett., Vol. 35, pp. 709-711, 1979.

13. J.G. Shaw and H.C. Card, "Electronic Transport at Grain Boundaries in Silicon", submitted to Phys. Rev. B, October (1982).

14. C.H. Seager, "Grain Boundary Recombination: Theory and Experiment in Silicon", J. Appl. Phys., Vol. 52, pp. 3960-3968, (1981).

15. D.J. Thomson, S.R. Mejia, and H.C. Card, "The Influence of Surface Preparation on Rectification in Aluminum-Polycrystalline Silicon Solar Cells", J. Power Sources, Vol. 7, pp. 191-194, (1982).

16. G. Baccarini, B. Ricco, and G. Spadini, "Transport Properties of Polycrystalline Silicon Films", J. Appl. Phys., Vol. 49, pp. 5565-5570, (1978).

17. H.C. Card, "The Photoconductivity of Polycrystalline Semiconductors", J. Appl. Phys., Vol. 52, pp. 3671-3673, (1981).

18. M.M. Mandurah, K.C. Saraswat, and T.I. Kamins, "A Model for Conduction in Polycrystalline Silicon - Part I: Theory", IEEE Trans. Electron. Dev., ED-28, (1981).

19. C.R. Crowell and S.M. Sze, "Current Transport in Metal-Semiconductor Barriers", Solid State Electron, Vol. 9, p. 1035, (1966).

20. S.M. Sze, Physics of Semiconductor Devices, 2nd Edition, Wiley-Interscience, New York, Chapter 5, (1981).

21. E.H. Rhoderick, Metal-Semiconductor Contacts, Clarendan Press, Oxford, (1978).

22. N.D. Arora, J.R. Hauser, and D.J. Roulston, "Electron and Hole Mobilities in Silicon as a Function of concentration and Temperature", IEEE Trans. on Electron. Dev., ED-29, pp. 292-295, (1982).

23. S.M. Sze, Physics of Semiconductor Devices, 2nd Edition, Wiley-Interscience, New York, p. 248, (1981).

24. L. Kazmerski, Polycrystalline and Amorphous Thin Films and Devices, Academic Press, New York, (1980).

25. Y.W. Lam, M.A. Green, and L.W. Davies, "Electrostatic Effects in Inversion-Layer MIS Solar Cells", Appl. Phys. Lett., Vol. 37, pp. 1087-1089, (1980).

26. P. Panayotatos and H.C. Card, "Recombination velocity at Grain Boundaries in Polycrystalline Silicon under Optical Illumination", IEEE Electron. Dev. Lett., EDL-1, pp. 263-266, (1980).

27. O.L. Krivanek, S. Isoda, and K. Kobayashi, "Lattice Imaging of a Grain Boundary in Crystalline Germanium", Phil. Mag., Vol. 36, pp. 931-940, 1977.

28. M.J. Buerger, The Precession Method in x-ray Crystallography, John Wiley & Sons, New York, (1966).

29. D. Redfield, "Selective Observation of Electriclly Active Grain Boundaries in Silicon", Appl. Phys. Lett., Vol. 38, pp. 174-176, (1981).

30. G.L. Miller, D.V. Lang, and L.C.Kimerling, "Capacitance Transient Spectroscopy", Ann. Rev. Mat. Sci., Vol. 7, pp. 377-448, (1977).

31. C.H. Seager, Grain Boundaries in Semiconductors, North-Holland, New York, (1982), pp. 85-98 and refs. to their early work within.

32. J. Werner, W. Jantsch, K.H. Froehner, and H.J. Queisser, in Ref. 31, pp. 99-104, (1982).

33. G.C. McGonigal, D.J. Thomson and H.C. Card, "Electronic Transport at Grain Boundaries in Silicon; Part II. Experiemnt", submitted to Physical Review B.

34. Murray R. Spiegel ed., Schaum's Handbook of Mathematical Formulas and Tables, p. 98, McGraw-Hill, New York, 1968.

35. M.M. Mandurah, K.C. Saraswat and C.R. Helms, "Dopant Segration in Polycrystalline Silicon", J. Appl. Phys., vol. 51, pp. 5755-5763, 1980.

36. E.H. Rhoderick, Metal-Semiconductor Contacts, p. 90, Clarendon Press, Oxford, 1978.

37. W.A. Anderson, G. Rajeswaran, K. Rajkanan and G. Hoeft, "A Revised Process to Increase Efficiency and Reproducibility in Cr-MIS Solar Cells", IEEE Elec. Dev. Lett., EDL-1, 128-130, 1980.

38. K.K. Ng and H.C. Card, "A Comparison of Majority- and Minority-Carrier Silicon MIS Solar Cells", IEEE Trans. on Elec. Dev., ED-27, 716-724, 1980.

39. J. Shewchun, M.A. Green and F.D. King, "Minority Carrier MIS Tunnel Diodes and Their Application to Electron- and Photovoltaic Energy Conversion - II, Experiment", Solid St. Electron., 17, 563-572, 1974.

40. R.B. Godfrey and M.A. Green, "High-Efficiency Silicon minMIS Solar Cells - Design and Experimental Results", IEEE Trans. on Elec. Dev., ED-27, 737-744, 1980.

41. D.S. Camporese, T.P. Lester and D.L. Pulfrey, "A Fine Line Shadow Mask for Inversion Layer Solar Cells", IEEE Elec. Dev. Lett., EDL-2, 61-63, 1981.

42. R.E. Thomas, R.B. North and C.E. Norman, "Low-Cost High-Efficiency MIS/Inversion Layer Solar Cells", IEEE Elec. Dev. Lett., EDL-1, 79-80, 1980.

43. M.A. Green, "Enhancement of Schottky Solar Cell Efficiency Above Its Semiempirical Limit", Appl. Phys. Lett., 27, 287-288, 1975.

44. A.K. Kong and M.A. Green, "The Efficiency of Grating Solar Cells", J. Appl. Phys., 49, 437-442, 1978.

45. A.W. DeGroot and H.C. Card, "Photovoltaic Processes in Metal-Semicrystalline Silicon Schottky Barriers and Implications for Grating Solar Cells", Solid St. Electron., in press.

46. H.C. Card, E.S. Yang and P. Panayotatos, "Peaked Schottky-Barrier Solar Cells by Al-Si Metallurgical Reactions", Appl. Phys. Lett., 30, 643-645, 1977.

47. D. Huber, R. Wahlich and D. Helmreich, "Typical Properties of Multicrystalline Silicon Material", Proc. of 14th IEEE Phot. Spec. Conf., San Diego, CA, 316-321, 1980.

48. Y.W. Lam, M.A. Green and L.W. Davies, "Electrostatic Effects in Inversion-Layer MIS Solar Cells", Appl. Phys. Lett., 37, 1087-1089, 1980.

49. H.C. Card, "One-Dimensional Analysis of Heat-Treated Aluminum-Silicon Junctions", in Metal-Semiconductor Contacts, Inst. of Phys., London, No. 22, 129-137, 1974.

50. H.C. Card and K.E. Singer, "In-Depth Auger Analysis of Aluminum-Silicon Interfacial Reactions", Thin Solid Films, 28, 265-268, 1975.

51. See, for example, M.A. Green, Solar Cells, Prentice-Hall, Englewood Cliffs, NJ, 1982, Chap. 5.

52. S.M. Sze, Physics of Semiconductor Devices, 2nd Edition, Wiley-Interscience, New York, Chapter 7, (1981).

53. E. Fabre, M. Mautref and A. Mircea, "Trap Saturation in Silicon Solar Cells", Appl. Phys. Lett., Vol. 27, pp. 239-241, Aug. 1975.

54. V.L. Dalal and A.R. Moore, "Design Considerations for High-Intensity Solar Cells", J. Appl. Phys., Vol. 48, pp. 1244-1251, March 1977.

55. C.T. Ho, R.O. Bell and F.V. Wald, "Enhancement of Diffusion Length in EFG Ribbon Solar Cells under Illumination", Appl. Phys. Lett., Vol. 31, pp. 463-465, October 1977.

56. A. Pogany, "Variation of Diffusion Length of Ribbon-Si Solar Cells with Light Intensity", Proc. 14th IEEE Phot. Spec. Conf., San Diego, CA, pp. 410-413, January 1980.

57. C.T. Ho and J.D. Mathias, "Effect of Short Wavelength Illumination of the Characteristic Bulk Diffusion Length in Ribbon Silicon Solar Cells", Solid St. Electron, Vol. 24, pp. 115-120, 1981.

58. R.D. Nasby, C.M. Garner, H.T. Weaver, F.W. Sexton and J.L. Rodriguez, "Characterization of p+nn+ Silicon Concentrator Solar Cells", Proc. 15th IEEE Phot. Spec. Conf., Kissimmee, Florida, pp. 132-137, 1981.

59. R.W. Sanderson and C.E. Backus, "The Behaviour of Silicon Concentrator Solar Cells Between 50 and 500 Suns", Proc. 15th IEEE Phot. Spec. Conf., Kissimmee, Florida, pp. 156-159, 1981.

60. V. Augelli, L. Vasanelli, M. Leo, R.A. Leo and G. Soliani, "Nonlinear Behaviour of the Short Circuit Current of a Solar Cell with Minority Carrier Lifetime Dependent on the Light Intensity", J. Appl. Phys., Vol. 53, pp. 1558-1562, March 1982.

61. V. Heine, "Dangling Bonds and Dislocations in Semiconductors", Phys. Rev., Vol. 146, pp. 568-570, June 1966.

62. W. Shockley and W.T. Read, Jr., "Statistics of the Recombination of Holes and Electrons", Phys. Rev., Vol. 87, pp. 835-842, September 1952.

63. R.N. Hall, "Electron-Hole Recombination in Germanium", Phys. Rev., Vol. 87, p. 387, 1952.

64. S.M. Sze, Physics of Semiconductor Devices, 2nd Ed. Chap. 14; Wiley, New York, 1981.

65. G.C. McGonigal, D.J. Thomson and H.C. Card, "Electronic Transport at Grain Boundaries in Silicon: Part II Experiment", Phys. Rev. B., to be published.

66. S.J. Fonash, Solar Cell Device Physics, Academic Press: New York, Chap. 4, pp. 166-168, 1981.

67. H.F. Matarê, Defect Electronics in Semiconductors, Wiley-Interscience: New York, Chap. 8, pp. 156-167, and Chap. 11, pp. 287-306, 1971.

APPENDIX A: Derivation of γ and estimation of its magnitude for present grain boundary samples.

The relationship between $\frac{d V_{do}}{dT}$ and $\frac{d\phi_p}{dT}$ for a uniform grain boundary is expressed by Eqn. (2.7).

$$\frac{dV_{do}}{dT} = - \gamma \frac{d\phi_p}{dT} \tag{7}$$

We now derive γ in terms of the interface-state density N_{is} at the grain boundary. Using Eqn. (2.12)

$$\frac{d Q_{is}}{dT} = - \frac{d(Q_1 + Q_2)}{dT} \tag{A1}$$

$$q N_{is} \frac{d \phi_b}{dT} \simeq - \frac{d(Q_1 + Q_2)}{d V_{do}} \cdot \frac{d V_{do}}{dT} \tag{A2}$$

for $V_1 = V_2 = 0$ and $V_{do} \gg V_T$. Also, from the fact that $\phi_b = V_{do} + \phi_p$,

$$q N_{is} \left(\frac{d\phi_p}{dT} + \frac{d V_{do}}{dT} \right) \simeq - \frac{d(Q_1 + Q_2)}{d V_{do}} \cdot \frac{d V_{do}}{dT} \tag{A3}$$

$$\frac{d V_{do}}{dT} = - \frac{1}{1 + \frac{d(Q_1 + Q_2)}{d V_{do}} \frac{1}{q N_{is}}} \cdot \frac{d \phi_p}{dT} \tag{A4}$$

Comparing Eqns. (A4) and (7) we have that

$$\gamma = \frac{1}{1 + \frac{d(Q_1 + Q_2)}{d\ V_{do}}\ \frac{1}{q\ N_{is}}} \qquad \text{(A5)}$$

In order to evaluate γ for our samples, we employ Eqns. (10) and (11) for Q_1 and Q_2 from which we obtain

$$\frac{d(Q_1 + Q_2)}{d\ V_{do}} = -\left[2\ q\ \varepsilon_s\ N_a(V_{do} - V_T)\right]^{1/2} 2q\ \varepsilon_s\ N_a$$

$$= -\left(\frac{2q\ \varepsilon_s\ N_a}{V_{do} - V_T}\right)^{1/2}$$

For our device B-10, $N_a = 3 \times 10^{21}\ m^{-3}$, $\varepsilon_s = 11.8\ \varepsilon_0$, $V_{do} \simeq 0.32$ V and $N_{is} \simeq 6\text{-}8 \times 10^{15}\ m^{-2}\ eV^{-1}$ at the equilibrium Fermi-level position ($\simeq E_v + 0.5$ eV) from which we obtain $\gamma \simeq 0.6$.

APPENDIX B: Derivation of Eqn. (3.7)

To derive Eqn. (3.7) we begin with the integral (3.5)

$$\exp(-\frac{V_{do}}{V_T}) = \int_0^\infty a(V_d)\, \exp(-\frac{V_d}{V_T})\, dV_d \qquad (B1)$$

we then substitute for $a(V_d)$ from Eqn. (2.6) which yields

$$\exp(-\frac{V_{do}}{V_T}) = \int_0^\infty \frac{1}{\sqrt{2\pi}\,\sigma} \exp\left[-\frac{V_d^2}{2\sigma^2} + \frac{2\langle V_d\rangle V_d}{2\sigma^2} - \frac{V_d}{V_T} - \frac{\langle V_d\rangle^2}{2\sigma^2}\right] dV_d \qquad (B2)$$

This integral is of the form

$$I = \int_0^\infty \exp-(a V_d^2 + b V_d + c)\, d V_d \qquad (B3)$$

where

$$a = \frac{1}{2\sigma^2} \qquad b = -\frac{\langle V_d\rangle}{\sigma^2} + \frac{1}{V_T} \qquad c = \frac{\langle V_d\rangle^2}{2\sigma^2} \qquad (B4)$$

From ref 34 integral (B3) has the solution

$$I = \frac{1}{2}\sqrt{\frac{\pi}{a}}\ \frac{1}{\sqrt{2\pi}\,\sigma} \exp(A)\operatorname{erfc}(B) \qquad (B5)$$

where

$$A = b^2 - 4ac/4a \qquad B = b/2\sqrt{a} \qquad (B6)$$

solving for A by substitution for a, b and c

$$A = \left[\left(-\frac{\langle V_d \rangle}{\sigma^2} + \frac{1}{V_T}\right) - 4\left(\frac{1}{2\sigma^2}\right)\left(\frac{\langle V_d \rangle^2}{2\sigma^2}\right)\right] \frac{\sigma^2}{2} \qquad \text{(B7)}$$

which simplifies to

$$A = \left(-\frac{\langle V_d \rangle}{V_T} + \frac{\sigma^2}{2V_T^2}\right) \qquad \text{(B8)}$$

solving for B by substitution for a and b we find

$$B = (-\langle V_d \rangle/\sigma^2 + 1/V_T)/2(1/\sqrt{2}\ \sigma) \qquad \text{(B9)}$$

which simplifies to

$$B = \frac{\sigma/V_T - \langle V_d \rangle/\sigma}{\sqrt{2}} \qquad \text{(B10)}$$

If we now substitute for a, (B8) and (B10) into (B5) the result is Eqn. (3.7)

$$\exp\left[-\frac{V_{do}}{V_T}\right] = \frac{1}{2} \exp\left[-\frac{\langle V_d \rangle}{V_T} + \frac{\sigma^2}{2V_T^2}\right] \operatorname{erfc}\left[\frac{\sigma/V_T - \langle V_d \rangle/\sigma}{\sqrt{2}}\right] \qquad \text{(B11)}$$

APPENDIX C: Explanation of the rise in activation energy (E_a) with applied bias voltage (V).

The explanation for the observed rise in E_a with V relies on three phenomena. First, the temperature dependence of the mobility. Second, the field dependence of the mobility. Third, the increase in the electric field with increasing V on the reverse-biased side of the grain boundary.

Consider the current density equation for grain boundary:

$$J = q\, N_v \frac{V_d\, V_r}{V_d + V_r} \exp(-\frac{\phi_b}{V_T}) \exp(\frac{V_1}{V_T}) \left[1 - \exp(-\frac{V}{V_T})\right] \qquad (C1)$$

If we now assume the Fermi level is pinned at the boundary then the only variation in J with applied voltage will arise in the $\frac{V_d\, V_r}{V_d + V_r}$ and the $\left[1 - \exp(-\frac{V}{V_T})\right]$ terms. For $V > V_T$ the voltage dependence will all be contained in the $\frac{V_d\, V_r}{V_d + V_r}$ term. For our case

$$V_d = \mu\, \varepsilon_1 \qquad V_r = \mu\, \varepsilon_2 \qquad (C2)$$

where ε_1 is the electric field at the grain boundary on the forward-biased side and ε_2 is that on the reverse-biased side. Under these assumptions, as V is increased V_r will increase and will eventually saturate at the scattering-limited velocity for holes.[52] We must now remember that when we are measuring E_a vs. V we employ data from two

different measurement temperatures. At the lower temperature the mobility will be higher; V_r therefore saturates at a lower voltage. The accelerated saturation of V_r at the lower temperature causes the $\frac{V_d V_r}{V_d + V_r}$ factor to depart more widely at large V than at small v, when comparing the two temperatures. Thus E_a increases with V.

APPENDIX D: Use of Photolithography Facilities.

The steps in the photolithographic process are as follows:

1) mask making
2) preparation of substrate
3) application of photoresist
4) prebaking of photoresist
5) exposure of photoresist
6) development of photoresist
7) post baking of photoresist
8) etching through photoresist mask
9) removal of photoresist.

Each step will be detailed.

1) Mask Making

The drawing to be reduced for a mask should be prepared on mylar (or suitable substitute) using black tape for drawing (eg. letraset letraline). The dimensions of the drawing can be calculated after the reduction ratio has been picked (micro filmers will make reductions of up to 36x). The reductions will come back as negatives on 35 mm film. This film should then be cut up and taped to clean glass slides with the emulsion away from the glass.

2) Preparation of Substrate

All substrates should be clean and very dry. One should also check that the photoresist is compatible with the substrate (eg. KTFR is not compatible with copper based alloys). The best procedure is to apply the photoresist immediately after removal of the substrate from a vacuum system or a furnace.

3) Application of Photoresist

a) Prepare photoresist for spinning. Resist should be consistency of syrup (if necessary add thinner).

b) Set controls of spinner to 4000 RPM and 40 sec duration.

c) Mount sample with properly sized O-ring.

d) Suck photoresist into clean syringe and attach filter.

e) Put several drops of resist on sample.

f) Spin on resist.

g) Remove substrate.

4) Prebaking Photoresist

a) Put sample on clean glass slide.

b) Have oven preheated to required temperature (eg. 100°C for KTFR).

c) Bake sample for required period (eg. 20 min for KTFR).

d) Remove sample.

5) Exposure of Photoresist

a) Make sure mask and sample are free of dust.

b) Align mask and sample under Xenon lamp.

c) Apply sufficient weight to make sure mask and sample are in close contact.

d) Start lamp set supply at 6 amps expose for about 6 min.

e) Stop lamp remove sample.

6) Developing of Photoresist

a) Set out 2 beakers of developer, 1 beaker of propanol, and 1 beaker of dion H_2O (KTFR).

b) To develop the photoresist pattern gently agitate the sample as follows:

1 min. first beaker of KTFR Developer

1 min. second

1 min. propanol

1 min. dion H_2O

c) Blow dry sample.

7) Post Baking of Photoresist

a) Put sample on clean glass slide.

b) Have oven preheated to required temperature (eg. 110°C for KTFR).

c) Bake sample for required period (eg. 20 in for KTFR).

d) Remove sample.

8) Etching of Sample

a) Find required etch, good sources for this material are:

Vossen and Kern, Thin Film Processes, and

Maissel and Glang, Handbook of Thin Film Technology,

McGraw Hill, Toronto, 1970.

b) Etch the sample and rinse with dion H_2O.

c) Blow dry sample.

9) Removal of Photoresist

a) Soak sample in Triclohalethylene for 5 min (KTFR only).

b) Agitate in sulfuric Acid (Acid heated to 40°C) until resist removed.

c) Thoroughly rinse in dion H_2O.

d) Blow sample dry.